J. Fluid Mech. (1974), *vol.* 64, *part* 1, *pp.* 129–165
Printed in Great Britain

A numerical study of turbulence transitions in convective flow

By BART J. DALY

Los Alamos Scientific Laboratory, University of California

(Received 3 February 1972 and in revised form 3 August 1973)

A turbulence representation, consisting of a generalized set of transport equations for the Reynolds stress tensor and the turbulence energy decay rate, is applied to the study of convective heat transport between parallel plates at moderate Rayleigh numbers, $5 \times 10^3 \leqslant Ra \leqslant 6{\cdot}4 \times 10^5$. A series of heat flux transitions, in good agreement with those observed experimentally, is detected in this study and found to correlate with changes in the turbulence structure. In the order of increasing Rayleigh number these structural changes correspond to: the transition from laminar to turbulent flow, the transition from low to locally high intensity turbulence, the transition to uniformly high intensity turbulence, and the transition from a buoyancy dominated turbulence to a shear dominated turbulence. An analysis is made of the effect of each of these transitions on the mechanism for heat transfer between the plates.

1. Introduction

When a fluid is confined between infinite parallel plates and heated from below, various forces may contribute to the heat transfer between the plates. Heat conduction provides the sole mechanism for small values of the buoyancy driving force (measured by the Rayleigh number Ra). For increasing values of Ra the heat transfer is influenced by the effects of two-dimensional fluid motions, three-dimensional motions and turbulent fluctuations. Transitions in heat flux are noted at the onset of each of these fluid motions, and additional transitions are observed to occur after the fluid becomes turbulent.

The heat flux transitions in the turbulent regime were first measured by Malkus (1954) in experiments with water and acetone. Since that time Willis & Deardorff (1967) and Krishnamurti (1970*a*, *b*) have performed similar experiments using fluids with Prandtl number Pr ranging from 0·71 to 8500. These workers observed a series of transitions at Rayleigh numbers that were very similar to those of Malkus, although there were particular transitions that did not fit the overall pattern. Despite these discrepancies, the picture that emerges is one of strong correlation in transition Rayleigh numbers for a large variety of fluids, indicating an evolution in turbulence structure with Ra that is relatively independent of Pr. No explanation of this phenomenon has as yet gained wide acceptance.

The purpose of the present study is to reproduce numerically the experimentally observed transitions, including the transition from laminar to turbulent

flow, and to relate these to the changes in turbulent structure. Calculations are performed for Rayleigh numbers in the range 5×10^3 to $6{\cdot}4 \times 10^5$ at a Prandtl number, 0·7, characteristic of air. These calculations make use of a coupled mean flow, turbulence representation that permits the interchange of energy between large and small scales of fluid motion. Only two-dimensional spatial variations are considered, but the calculations do include the experimentally observed (Lipps & Somerville 1971; Willis, Deardorff & Somerville 1971) effect of increased wavelength of flow circulation with Ra.

An auxiliary purpose of this study is to provide an additional test of a transport representation of turbulence that had previously been applied only to shear flow problems. In Daly & Harlow (1970) a generalized set of transport equations was proposed to represent transient, incompressible turbulent flow. Applications were made to the calculations of turbulence distortion in a contracting tunnel and to the calculation of turbulent channel flow. Using the same set of turbulence parameter values, both studies were in good agreement with experimentally measured turbulence details. Except for those additional parameters needed to describe the effects of buoyancy (plus one additional term described below) the representation used here is identical to that of the earlier studies.

2. Limitations of the numerical approach

2.1. *Previous investigations*

There have been many numerical studies of laminar Bénard convection. With few exceptions (Chorin 1966, 1968; Lipps & Somerville 1971) these have been limited to two-dimensional motions and, in most cases, to circulations of wavelength approximately twice the plate separation distance h. These studies are generally in good agreement among themselves, but predict a heat flux between the plates that is greater than that measured experimentally. Recent evidence (Lipps & Somerville 1971; Willis *et al.* 1971) indicates that this discrepancy is a direct consequence of the two-dimensional and wavelength constraints imposed by the numerical solution. Willis *et al.* observe an increase of wavelength with Ra, the rate of increase depending on Ra, Pr, initial conditions, the method of taking measurements and three-dimensional interactions.

Some two-dimensional numerical studies have employed finite-difference meshes of large lateral extent in order to allow the circulation to evolve to a preferred size. Deardorff & Willis (1965) used a grid of width eight times its height and Lipps & Somerville (1971) used grids of aspect ratio six and eighteen. In none of these cases did they observe a wavelength increase, and in some instances the calculated wavelength was considerably less than $2{\cdot}0h$, which is approximately the observed wavelength at the onset of convection. However, when Lipps & Somerville extended their study to three-dimensional calculations, this trend was reversed. In calculations appropriate to air at $Ra = 4000$ and to water at $Ra = 8000$ they measured wavelengths of $3{\cdot}0$ and $2{\cdot}8h$, respectively. While these values are slightly larger than those observed experimentally ($2{\cdot}8$ and $2{\cdot}3h$), they do provide a strong indication that three dimensions are necessary for accurate numerical calculations of roll wavelength.

There appears to be ample evidence to indicate that the discrepancy between numerical and experimental wavelengths leads to the discrepancy in heat flux observations. Thus Willis *et al.* (1971) have found that, when the two-dimensional calculation wavelength is *forced* to correspond to experimental values for air, good heat flux correlation is obtained. Similar good agreement with experiment was obtained in two-dimensional calculations by Lipps & Somerville (1971) for $Pr = 200$, by forcing the wavelength to correspond to that measured by Rossby (1966). These results indicate that the neglect of three dimensionality in numerical calculations is not necessarily a crucial restriction if one is careful to preserve the experimentally observed variation of circulation wavelength with Ra.

2.2. *The present study*

The calculations presented in this paper are, like most of those mentioned above, restricted to the consideration of a single, infinitely long, two-dimensional roll. The lateral boundaries of the calculation mesh are lines of symmetry, so that the single roll has identical neighbours of opposite circulation. These calculations include the effect of the increased circulation wavelength that occurs with Ra and that was found to be extremely important in obtaining good correlation between numerical and experimental heat flux measurements.

This investigation differs from most of the previous ones in that it extends to Ra values for which the flow is observed to be turbulent. Solutions are obtained by coupling the Navier–Stokes and heat equation with a system of transport equations for transient anisotropic three-dimensional turbulence. From initial conditions these coupled equations are then integrated through time to steady state. The steady-state results are independent of initial conditions and, for fixed boundary conditions and Prandtl number, depend only upon the Rayleigh number.

This model of the flow represents a considerable idealization of three-dimensional convective flow. For the values of Ra under consideration here, the rolls display numerous bends, variations in shape and occasional terminations. Furthermore, they are not fixed in space but slowly migrate throughout the region between the plates, so that there is no steady state. Therefore, the usefulness of the numerical study, which ultimately must be demonstrated, can only be attributable to the fact that the gross properties of the flow are not strongly affected by the three-dimensional and time-varying nature of the fluid motion. Indeed, in the laminar regime it was found that the neglect of these effects was not critical as long as one was careful to force the circulation wavelength to correspond to that observed experimentally (§ 2.2). Even at the higher Ra considered here, it seems reasonable that the gross dynamics of the flow will be determined by the vertical motions of the fluid and be less influenced by the lateral oscillations and migrations of the flow. Therefore the neglect of these three-dimensional effects should not obscure the changes in turbulent structure that this study examines.

3. The equations

3.1. *Distinction between mean flow and turbulence*

The significance of the turbulence transport equations can be considered in a context that is independent of the numerical or analytical approximations used for obtaining solutions. For any time-varying fluid flow in arbitrary geometry, the coupled turbulence and mean flow equations describe the dynamical evolution from given initial conditions, subject to prescribed boundary conditions. Relatively few parameters enter into these specifications, many fewer than the detailed degrees of freedom could conceivably allow. These parameters are of two types, the 'universal' parameters occurring in the turbulence transport and mean flow equations, and the quantities that specify the initial and boundary conditions.

It is a remarkable fact that complex turbulent flows can be accurately described with such a paucity of specifications. There is no need to describe the precise initial state of the velocity field at every point, only a small number of low order moments are required. An analogous situation arises in gas dynamics. There, the specifications can be given with sufficient precision in terms of a small number of low order moments, without requiring the initial conditions for every molecule.

The key to understanding this requirement for minimum specification lies in the existence of a distribution function whose form tends so strongly toward equilibrium that no specification of details is required. For molecular dynamics we refer to the Maxwell–Boltzmann distribution, from which slight deviations can be described by means of the small number of parameters that are contained in the Chapman–Enskog theory. For turbulence, this function is not yet known, especially for circumstances that induce slight deviations from equilibrium.

Just as the Navier–Stokes equations can be postulated on the basis of invariance principles, so also can the turbulence transport equations. The precise knowledge of the structure of the distribution function is not required. Application of the equations to a specific problem automatically accounts for the distinction between mean flow and fluctuations, without requiring, or even allowing for, a precise description of the split. In particular, it is not necessary to introduce such artificial entities as 'short time, local averaging' or 'averaging over a volume small compared with the mean flow structure'. While these may be useful for heuristic purposes, the general spirit of Liouville theory shows that they are never necessary.

Thus the conclusion is that whenever the turbulence transport equations are successful in describing real flow processes, it is because there exists a nearly universal subsection of the entire distribution function to which the turbulence equations apply, the rest being related to the mean flow equations. It remains as a significant research project to determine this universal part, just as it remained, after Stokes's stress tensor postulates, for later investigators to derive the Chapman–Enskog distribution functions for molecular dynamics.

3.2. *The turbulence representation*

The turbulence representation employed in this study is identical to that described by Daly & Harlow (1970), except for one addition to the pressure–velocity correlation term. This representation consists of transport equations for the Reynolds stress tensor, $R_{ij} = \overline{u_j' u_j'}$, and the contracted energy decay tensor, $D = D_{ii} = \frac{1}{2}\overline{(\partial u_i'/\partial x_k)^2}$. These equations have been derived from the fluctuating Navier–Stokes equations for a viscous, incompressible fluid, with approximations for the higher order moments that arise in that derivation. Rather than repeating the details of those approximations, we refer the reader to the earlier paper and present only the final transformed equations. In summation convention form these are written:

$$\frac{\partial R_{ij}}{\partial t} + u_k \frac{\partial R_{ij}}{\partial x_k} = -R_{ik}\frac{\partial u_j}{\partial x_k} - R_{jk}\frac{\partial u_i}{\partial x_k} + \frac{\alpha}{Pr}\frac{\partial}{\partial x_k}\left(\frac{s^2 R_{kl}}{\Delta}\frac{\partial R_{ij}}{\partial x_l}\right) + \Phi_{ij}$$
$$+ \frac{\theta}{Pr}\left[\frac{\partial}{\partial x_j}\left(\frac{s^2 q}{\Delta}\frac{\partial R_{ik}}{\partial x_k}\right) + \frac{\partial}{\partial x_i}\left(\frac{s^2 q}{\Delta}\frac{\partial R_{jk}}{\partial x_k}\right)\right]$$
$$+ Pr\frac{\partial^2 R_{ij}}{\partial x_k^2} - \frac{2Pr\Delta}{s^2}R_{ij} - \frac{Ra\,Pr\,\tau s^2}{\Delta}(\hat{l}_i R_{jk} + \hat{l}_j R_{ik})\frac{\partial T}{\partial x_k}, \quad (1)$$

$$\frac{\partial D}{\partial t} + u_k \frac{\partial D}{\partial x_k} = -\frac{g(\xi)\Delta}{s^2}R_{jk}\frac{\partial u_j}{\partial x_k} + \frac{1}{Pr}\frac{\Delta}{s^2}\frac{\partial}{\partial x_k}\left(\frac{s^2 R_{kl}}{\Delta}\frac{\partial q}{\partial x_l}\right) + \frac{1}{Pr}\frac{\partial}{\partial x_k}\left(\frac{s^2 R_{kl}}{\Delta}\frac{\partial D}{\partial x_l}\right)$$
$$+ \frac{\theta}{Pr}\frac{\partial}{\partial x_j}\left(q\frac{\partial R_{jl}}{\partial x_l}\right) + Pr\frac{\partial^2 D}{\partial x_k^2} - \frac{2Pr\Delta' D}{s^2} - Ra\,Pr f(\xi)\hat{l}_j R_{jl}\frac{\partial T}{\partial x_l} \quad (2)$$

(where the equations have been made dimensionless by the distance and temperature difference between the plates h and δT, and by the thermal diffusivity κ), for mean velocity u_k, turbulence energy $q = \frac{1}{2}R_{kk}$, scale of the energy carrying eddies $s = (\Delta q/D)^{\frac{1}{2}}$, fluctuating pressure–velocity gradient correlation, with zero contraction (detailed below) Φ_{ij}, mean temperature T, Prandtl number $Pr = \nu/\kappa$ (molecular kinematic viscosity ν), Rayleigh number $Ra = (\beta g h^3 \delta T)/(\kappa\nu)$, volumetric coefficient of expansion β, gravitational acceleration magnitude g.

$$\hat{l}_i = \begin{cases} 0 & \text{for } i = 1, 2, \\ 1 & \text{for } i = 3. \end{cases}$$

In addition, there are a number of coefficients, some fixed constants and others that are functions of the turbulence Reynolds number $\xi = s(2q)^{\frac{1}{2}}/\nu$. The constants, all of which appear in the R_{ij} equation, are: the coefficient of the turbulent diffusion term α, the coefficient of the conservative pressure–velocity correlation θ, the coefficient of the buoyancy creation term τ. The terms that are functions of ξ are: the coefficient of the R_{ij} decay term, also used in the definition of s and in moment approximations $\Delta(\xi)$, the coefficient of the D decay term $\Delta'(\xi)$, the coefficient of the D shear creation term $g(\xi)$, the coefficient of the D buoyancy creation term $f(\xi)$.

The pressure–velocity correlation term Φ_{ij} has vanishing contraction. Its effect therefore is limited to non-isotropic turbulence, in which it contributes to

a redistribution of energy among the components and to variations of the shear stress magnitude. It has the form

$$\Phi_{ij} = -\frac{\omega Pr\Delta}{s^2}(R_{ij}-\tfrac{1}{3}R_{kk}\delta_{ij})+\frac{2\mu q}{5}\left(\frac{\partial u_i}{\partial x_j}+\frac{\partial u_j}{\partial x_i}\right)$$
$$+Ra\,Pr\frac{s^2 q}{10\Delta}\left(\hat{l}_i\frac{\partial T}{\partial x_j}+\hat{l}_j\frac{\partial T}{\partial x_i}-\tfrac{2}{3}\hat{l}_k\frac{\partial T}{\partial x_k}\delta_{ij}\right)-\frac{\zeta Pr\Delta}{2s^2}(P_{il}R_{lj}+P_{jl}R_{li}-\tfrac{2}{3}P_{lm}R_{lm}\delta_{ij})$$
$$-\Omega\left(R_{ik}\frac{\partial u_k}{\partial x_j}+R_{jk}\frac{\partial u_k}{\partial x_i}-R_{ik}\frac{\partial u_j}{\partial x_k}-R_{jk}\frac{\partial u_i}{\partial x_k}\right), \quad (3)$$

where $$\omega = \omega_0-\frac{\omega_1 s^2}{Pr\Delta q}R_{kl}\frac{\partial u_k}{\partial x_l}, \quad \delta_{ij}=\begin{cases}1 & \text{for } i=j,\\ 0 & \text{for } i\neq j,\end{cases}$$

and ω_0, ω_1, μ, ζ and Ω are constants. The ω term, which tends to produce isotropy, was originally proposed by Rotta (1951). The μ term, derived independently by Crow (1968) and Harlow & Hirt (1969), relates pressure–velocity correlations to mean flow shear in a manner that tends to counteract the shear creation terms in (1). The next two terms in (3) were also derived by Harlow & Hirt (1969). The first of these represents the effect of temperature fluctuations in producing fluctuations in pressure, while the second is a wall effect term that accounts for the transfer of energy from the normal to the transverse directions in the vicinity of rigid walls. The tensor P_{ij} provides the angular relationships between the directions **i** and **j** and the normal to the wall, as well as a weighting that falls off rapidly with distance from the wall (Daly & Harlow 1970, (20)–(22)).

The final term in (3) is the sole addition to the turbulence theory presented here. It includes terms proportional to the shear creation terms of (1) as well as other shear terms that do not arise in the derivation of (1). It permits the exchange of energy among components in a way that amounts to additional shear creation terms for some components and sinks for others. In this capacity it can be an extremely important contributor in non-isotropic flows involving large mean flow shears. This term is not original in the present turbulence representation, but was proposed by Chou (1945*a*, *b*) and Rotta (1951), who showed that it could be obtained from the pressure–velocity derivative correlation.

Equation (1) permits all possible forms for the decay term between the extremes of 'local isotropy' and proportionality to Reynolds stress. To see this, consider the following two terms from that equation:

$$-\frac{\omega\, Pr\Delta}{s^2}(R_{ij}-\tfrac{1}{3}R_{kk}\delta_{ij})-\frac{2\,Pr\Delta}{s^2}R_{ij}.$$

Written in this form the decay term appears proportional to Reynolds stress, but by a rearrangement of terms it can also be written as

$$-\frac{(\omega+2)\,Pr\Delta}{s^2}(R_{ij}-\tfrac{1}{3}R_{kk}\delta_{ij})-\frac{2\,Pr\Delta}{3s^2}R_{kk}\delta_{ij},$$

in which form the decay is isotropic. Thus, a variation of the relative amounts of the two forms of decay can be accomplished through changes in the coefficient, ω.

3.3. *The mean flow*

The mean flow equations for an incompressible fluid, with the Boussinesq approximation, can be written as follows:

$$\frac{\partial u_k}{\partial x_k} = 0, \tag{4}$$

$$\frac{\partial u_j}{\partial t} + \frac{\partial u_j u_k}{\partial x_k} = -\frac{\partial \phi}{\partial x_j} - \hat{l}_j[1 - Ra\,Pr\,(T - T_0)] + \frac{\partial}{\partial x_k}\left(Pr\frac{\partial u_j}{\partial x_k} - R_{jk}\right), \tag{5}$$

$$\frac{\partial T}{\partial t} + \frac{\partial u_k T}{\partial x_k} = \frac{\partial}{\partial x_k}\left(\frac{\partial T}{\partial x_k} + \frac{\tau s^2 R_{kl}}{\Delta}\frac{\partial T}{\partial x_l}\right), \tag{6}$$

for the pressure divided by constant density ϕ, and constant reference temperature T_0. Also τ, the coefficient of turbulent diffusion of T, is the same as the buoyancy creation coefficient in (1).

3.4. *Application to the turbulent heat flux problem*

The fluid is confined between two rigid, insulated, horizontal plates located at $z = 0$, 1 and maintained at temperatures, $T = +\frac{1}{2}$, $-\frac{1}{2}$, respectively. In the x direction the motion is contained by planes of symmetry at $x = 0$ and $x = l/h$, so that the flow is periodic in x, with period $2l/h$. Computer limitations require that we restrict our attention to two-dimensional flows, and we therefore assume all quantities to be constant in y and take $u_2 \equiv 0$. The constancy in y implies that (1) contains no creation terms for the components R_{12} and R_{23}, so that these, if not initially zero, would rapidly decay to zero. However, this is not true of the component R_{22}, which receives contributions from the intercomponent coupling terms, Φ_{12} and Φ_{23}.

There is an additional symmetry that could be included in this problem formulation. It arises from the fact that (1)–(6) are all symmetric about the midpoint of the domain, $(l/2h, \frac{1}{2})$. By taking advantage of this fact, an identical solution could be obtained by solving the problem over one half the present region of interest. Instead, we used this symmetry requirement as a test on the accuracy of the numerical solution.

The boundary conditions can be summarized as follows:

$$\left.\begin{aligned}
&u_1(0,z) = u_1\left(\frac{l}{h}, z\right) = u_1(x,0) = u_1(x,1) = 0,\\
&\frac{\partial}{\partial x}[u_3(0,z)] = \frac{\partial}{\partial x}\left[u_3\left(\frac{l}{h}, z\right)\right] = u_3(x,0) = u_3(x,1) = 0,\\
&\frac{\partial}{\partial x}[T(0,z)] = \frac{\partial}{\partial x}\left[T\left(\frac{l}{h}, z\right)\right] = 0 \quad (T(x,0) = +\tfrac{1}{2}, \quad T(x,1) = -\tfrac{1}{2}),\\
&\frac{\partial}{\partial x}[R_{ij}(0,z)] = \frac{\partial}{\partial x}\left[R_{ij}\left(\frac{l}{h}, z\right)\right] = R_{ij}(x,0) = R_{ij}(x,1) = 0 \quad (ij = 11, 22, 33),\\
&R_{13}(0,z) = R_{13}\left(\frac{l}{h}, z\right) = R_{13}(x,0) = R_{13}(x,1) = 0,\\
&\frac{\partial}{\partial x}[D(0,z)] = \frac{\partial}{\partial x}\left[D\left(\frac{l}{h}, z\right)\right] = 0 \quad (D \to \infty \quad \text{as} \quad z \to 0, 1).
\end{aligned}\right\} \tag{7}$$

As discussed by Daly & Harlow (1970), the last condition, strictly speaking, applies only in the laminar sublayer. Its implementation in a numerical study involves a certain amount of compromise, in view of the fact that the flow in the laminar sublayer usually is not well resolved. Good results were obtained in the study of channel-flow turbulence (Daly & Harlow 1970) through the use of a modified form of a result obtained by Harlow & Hirt (1969) appropriate in the near vicinity of the wall. In terms of the value of D in the first calculational cell, $D_1 = D(x, \frac{1}{2}\delta z)$, their result gives, for $z < \frac{1}{2}\delta z$,

$$D = D_1 \left(\frac{2}{\delta z}\right)^{n-2} z^{n-2}, \tag{8}$$

where $n = 1{\cdot}4372$. The modification used in the channel flow study as well as the present one is to take $n = 1{\cdot}6$ rather than $1{\cdot}4372$.

3.5. *Parameter values*

This study makes use of the same set of functional expressions and parameter values used by Daly & Harlow (1970), viz.

$$\omega_0 = \omega_1 = \alpha = 1{\cdot}0, \quad \mu = \theta = 0{\cdot}0,$$

$$\zeta = 0{\cdot}14, \quad P_{ij}(x,z) = \begin{cases} 0{\cdot}0 & (ij \neq 33), \\ \left[\dfrac{s(x,z)}{z}\right]^2 & (ij = 33), \end{cases}$$

$$\Delta(\xi) = \begin{cases} \xi & (\xi \geqslant 5), \\ 5 & (\xi < 5), \end{cases} \quad \Delta'(\xi) = \begin{cases} 2\Delta & (\xi \geqslant 5), \\ 1{\cdot}4\Delta & (\xi < 5), \end{cases} \quad g(\xi) = \begin{cases} 0{\cdot}8 & (\xi \geqslant 5), \\ 1{\cdot}0 & (\xi < 5). \end{cases} \tag{9}$$

In addition, several new quantities are introduced. Their values are

$$\tau = 0{\cdot}8, \quad \Omega = 0{\cdot}2, \quad f(\xi) = \begin{cases} 1{\cdot}7 & (\xi \geqslant 5), \\ 1{\cdot}0 & (\xi < 5). \end{cases} \tag{10}$$

In applications of this turbulence representation to the problems of turbulence distortion in a non-uniform tunnel (Harlow & Romero 1969) and to turbulent channel flow (Daly & Harlow 1970), considerable attention was given to the sensitivity of results to variations of the values of the parameters (9). Most of these findings apply equally well to the current study; the interested reader is referred to those references for details. The effect of varying the newly introduced parameter values (10) is considered in appendix B for a flow situation that provides a severe test of the sensitivity to these parameters. These tests show that the numerical measurements are particularly sensitive to variations in τ. This is not surprising, since τ plays the double role of turbulent heat diffusion coefficient in (6) and turbulent buoyancy creation coefficient in (1). Thus, this coefficient controls the entire coupling between the turbulent flow and the driving mechanism. The effect of varying $f(\xi)$ is much less important, while changes in Ω have practically no effect on results.

Of particular interest in this study is the representation of the transition from low to high intensity turbulence, because this transition is closely related to the

heat flux transitions to be discussed in § 3.6. The decay rate coefficients $\Delta(\xi)$ and $\Delta'(\xi)$ of the R_{ij} and D equations have a strong influence on the nature of the transition in turbulence regimes, so we briefly review here the basis for the formulation of these terms shown in (9). For isotropic turbulence it can be shown (Hinze 1959, p. 179) that the dissipation of turbulence energy q can be written $-10\nu q/\lambda^2$, where λ is the turbulence dissipation scale. In our formulation this dissipation term is written $-2\nu\Delta q/s^2$, where s is the scale of the energy carrying eddies. Thus

$$\frac{5}{\lambda^2} = \frac{\Delta}{s^2} = \frac{D}{q}, \tag{11}$$

where the last comes from our definition of s, § 3.2.

Consider the two extreme values for $\Delta(\xi)$ given in (9). For low intensity turbulence ($\xi < 5$ in our representation) dissipation occurs in eddies of size of the order of the energy carrying eddies (i.e. $\lambda = s$), so that $\Delta = 5$ from (11). For high Reynolds numbers the Kolmogorov theory of turbulent microstructure asserts that the dissipation is approximately equal to the work done by the energy carrying eddies (Hinze 1959, p. 185), i.e.

$$-\nu\overline{\left(\frac{\partial u_i'}{\partial x_k}\right)^2} \propto -\frac{(2q)^{\frac{3}{2}}}{s}. \tag{12}$$

In the present turbulence representation, this term is

$$-\nu\overline{\left(\frac{\partial u_i'}{\partial x_k}\right)^2} = -\frac{2\nu\Delta q}{s^2}, \tag{13}$$

where

$$\Delta = \xi = \frac{s(2q)^{\frac{1}{2}}}{\nu}$$

at high intensity. The constant of proportionality relating (12) and (13) has been chosen equal to unity, consistent with other assumptions of the form (13) that are used in the derivation of (1) and (2).

The formulation for $\Delta'(\xi)$ in (9) is unchanged from that of Daly & Harlow (1970), but our interpretation of the origin of this term has been modified by Rodi (1971) and Lumley (1970). In particular, the latter showed that, for homogeneous turbulence, the decay term in (2), $-2\,Pr\,\Delta' D/s^2$, represents the combined contribution of the two terms (see Daly & Harlow 1970, (14))

$$-\overline{\frac{\partial u_j'}{\partial x_l}\frac{\partial u_k'}{\partial x_l}\frac{\partial u_j'}{\partial x_k}} \quad \text{and} \quad -\nu\overline{\left(\frac{\partial^2 u_j'}{\partial x_k \partial x_l}\right)^2}. \tag{14}$$

The first of these was modelled by Daly & Harlow (1970) as

$$\overline{\frac{\partial u_j'}{\partial x_l}\frac{\partial u_k'}{\partial x_l}\frac{\partial u_j'}{\partial x_k}} = \frac{\Delta}{s^2}\frac{\partial}{\partial x_k}\left(\frac{s^2 R_{kl}}{\nu\Delta}\frac{\partial q}{\partial x_l}\right), \tag{15}$$

but this cannot be complete, since the right-hand side vanishes for homogeneous turbulence, whereas the left-hand side does not. Thus, following Lumley (1970), we now believe that there is an additional contribution to the right-hand side of (15) of the form

$$-(\text{constant})\,Pr\,\Delta D/s^2.$$

Combining this with a similar contribution from the second term in (14) gives the decay term in (2):

$$-2\,Pr\,\Delta' D/s^2.$$

In the case of high Reynolds number flow in grid turbulence, Lumley (1970) obtains a result that, written in our notation, gives $\Delta' = 2\Delta$. This agrees with our high Reynolds number value in (9).

Results from Batchelor & Townsend's (1948) experimental studies of grid turbulence also support the expression for $\Delta'(\xi)$ in (9). They measure the temporal variation of the turbulence dissipation scale during the initial (high intensity) state of decay, as well as in the final (low intensity) state, finding

$$\frac{\partial \lambda^2}{\partial t} = \begin{cases} 10\nu \text{ initial state,} \\ 4\nu \text{ final state.} \end{cases} \tag{16}$$

These measurements can be interpreted in terms of our formulation, using (11). Thus

$$\frac{\partial \lambda^2}{\partial t} = 5\frac{\partial}{\partial t}\left(\frac{s^2}{\Delta}\right) = 5\frac{\partial}{\partial t}\left(\frac{q}{D}\right). \tag{17}$$

For this decay problem the appropriate equations for q and D are

$$\partial q/\partial t = -2\nu D, \quad \partial D/\partial t = -2\nu\Delta' D/s^2. \tag{18}$$

Using (18) in (17) gives

$$\partial \lambda^2/\partial t = 10\nu(\Delta'/\Delta - 1).$$

Comparing this result with (16), one obtains initial and final state values of Δ' that are in exact agreement with the high and low intensity values of Δ', respectively, in (9).

The expressions in (9) and (10) show a rapid transition from low to high intensity turbulent regimes; indeed, for $\Delta'(\xi)$, $g(\xi)$ and $f(\xi)$ the change is discontinuous. Batchelor & Townsend (1948) did not report discontinuous changes in turbulence parameters, but, in the one experiment for which they did attain final period decay, the transition occurred quite rapidly. For this experiment their turbulence Reynolds number $Re_\lambda = u'\lambda/\nu$ decreased from an initial value of 7·3 to 5·0 at the onset of final period decay, which occurred at approximately 400 mesh widths downstream from the grid. The relationship between Re_λ and our turbulence Reynolds number ξ is $\xi = 3^{\frac{1}{2}} Re_\lambda$ at low intensity. Our transition value $\xi = 5$ may therefore be somewhat low. On the other hand, a second experiment, for which $Re_\lambda = 8{\cdot}5$ in the initial period, did not reach final period decay, even though Re_λ decreased to ~ 4. Indeed, as Batchelor & Townsend point out, a simple Reynolds number criterion is probably not correct. More information about low intensity turbulence is needed to determine this transition accurately.

3.6. *Numerical calculations*

Two series of numerical calculations were performed for

$$5 \times 10^3 \leqslant Ra \leqslant 6{\cdot}4 \times 10^5, \quad Pr = 0{\cdot}7,$$

to examine the effect of the wavelength of the large-scale motions on the turbu-

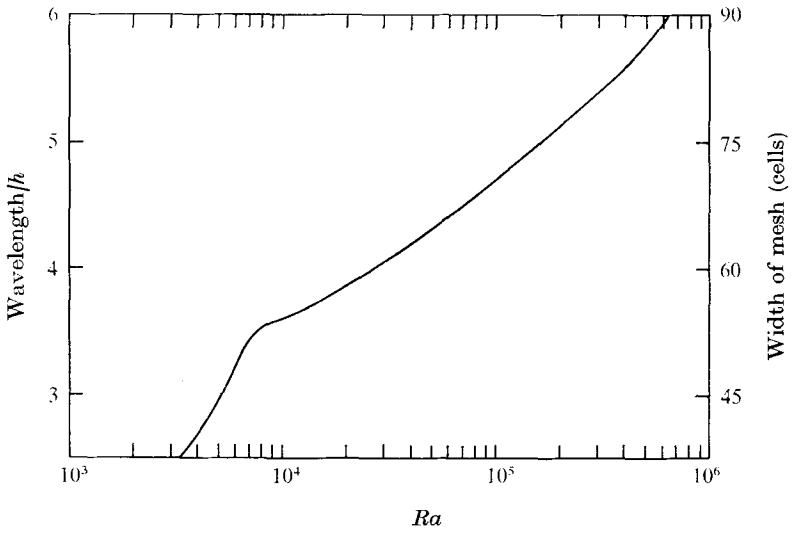

FIGURE 1. Non-dimensional roll wavelength and corresponding finite-difference mesh width as functions of Rayleigh number. For $Ra < 3 \times 10^4$, wavelengths are obtained from experimental measurements of Willis *et al.* (1971). Extrapolation to higher Ra used data of Deardorff & Willis (1965, 1967).

lence–mean flow coupling and the heat flux between the plates. In one series the calculation mesh was square, so that the wavelength of the large motions was twice the plate separation distance. In the second series the width of the mesh was varied, to represent the experimentally observed increase of roll wavelength with Ra, as indicated in figure 1.

Figure 1 shows the experimentally observed non-dimensional wavelength as a function of Rayleigh number. The wavelength increases rapidly until $Ra = 8 \times 10^3$, where there is a transition to a slower rate of increase. The data for $Ra < 3 \times 10^4$ were obtained from an extensive series of experiments by Willis *et al.* (1971), and are probably quite reliable. However, at higher Rayleigh numbers there are much less data available. There is a single wavelength measurement at $Ra = 1{\cdot}6 \times 10^5$ by Deardorff & Willis (1965), and this datum point is somewhat questionable owing to the possibility of two-dimensional constraints on the experimental apparatus. In addition, a rough wavelength estimate can be obtained from the spectra of fluctuating quantities at $Ra = 6{\cdot}3 \times 10^5$ provided by Deardorff & Willis (1967). Despite the lack of quantitative information for $Ra > 3 \times 10^4$, the wavelength variation indicated in figure 1 was used in the numerical calculations as a qualitative representation of this important physical phenomenon.

Steady-state numerical solutions of (1)–(6) were obtained as limits of transient problems. At low Rayleigh numbers a laminar steady state was obtained first. Then a low intensity turbulence field was introduced, and the equations were integrated through time to a new steady state, which would correspond to the laminar solution if the turbulence decayed away. However, once the Ra for transition to turbulence had been determined, the separate laminar flow solution

was often deleted at higher Rayleigh numbers, and a single turbulent solution was developed from initial conditions. The same steady-state solution was obtained under either procedure.

Finite-difference solutions were obtained by applying the Simplified Marker and Cell technique (Amsden & Harlow 1970*a*, *b*) for incompressible flow to (4) and (5), coupled with space-centred differencing of (1), (2) and (6). Calculations were made on the CDC 6600 and 7600 computers, with output processed on the Stromberg Carlson model 4020 microfilm recorder. The details of the numerical calculations are discussed in appendix A.

4. Results

4.1. *Comparison of heat flux measurements using fixed and variable calculation meshes*

Figure 2 shows the variation of steady-state Nusselt number Nu (a dimensionless measure of heat flux), with Rayleigh number (as calculated in this study and measured by several experimenters). The dashed curve in the figure was drawn by the author from experimental measurements with water by Rossby (1966) and Silveston (1958). The triangles mark Nusselt number measurements in air by Mull & Reiher (1930). The solid lines show the calculated results: the curve through squares gives the values of Nu obtained with a fixed, 30×30 cell, finite-difference mesh, while the curve through circles shows those calculated using a mesh of fixed height, 30 cells, and varying width. The width of the mesh increases with Ra as shown in figure 1. The hollow circles show values of Nu measured in variable width calculations, in which the flow was constrained to be non-turbulent.

The calculated Nu values in figure 2 are in good agreement with numerical results obtained under similar wavelength conditions by other investigators (Plows 1968; Willis *et al.* 1971) for $Ra \lesssim 2 \times 10^4$, the upper limit for most numerical studies. Willis *et al.* (1971) found that they could obtain good Nu correlation with experimental data for air when they forced their circulation wavelength to correspond to the experimentally measured wavelength (§ 2.1), whereas much poorer correlation was obtained using a fixed numerical wavelength. We observe the same results when we use their wavelength measurements (figure 1) to determine the width of our variable mesh.

Thus the calculated variable wavelength results in figure 2 have been shown to be in good agreement with experimental measurements for air for

$$5 \times 10^3 \leqslant Ra \leqslant 2 \times 10^4.$$

This is confirmed by the agreement with Mull & Reiher's (1930) measurement at $Ra = 9 \times 10^3$ in figure 2. For larger values of Ra, however, the situation is less clear. The fixed mesh turbulent calculations predict a Nu variation with Ra that departs rapidly from experiment for $Ra > 4 \times 10^4$, showing that this assumption gives a poor approximation to reality for these values of Ra. But a two-dimensional, variable wavelength approximation for the mean motion, coupled with the turbulence representation, cannot be expected to produce an accurate

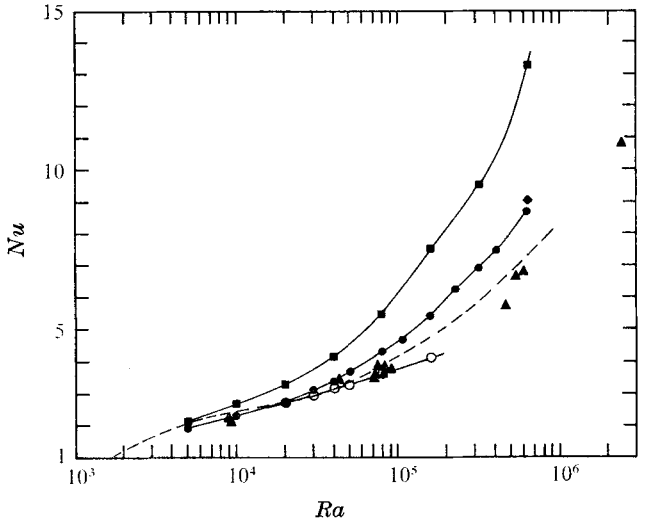

FIGURE 2. Variation of steady-state Nusselt number with Rayleigh number. Experimental results: ---, drawn by the author from measurements in water by Rossby (1966) and Silveston (1958); ▲, measurements in air by Mull & Reiher (1930). Numerical results: —■—, square mesh; —●—, variable width mesh with turbulence; —○—, variable width mesh without turbulence; ◆, test of smaller width mesh.

prediction of heat flux at these high Ra either. Three-dimensional effects, which Willis *et al.* (1971) and the present calculations show can be neglected to a good approximation for $Ra < 2 \times 10^4$ if the effect of wavelength variation with Ra is included, can no longer be ignored if $Ra > 2 \times 10^4$. At the smaller Ra, these three-dimensional motions consist of lateral migrations, sinuous oscillations and occasional bends in rolls that otherwise maintain their two-dimensional identity. As the Ra is increased, these three-dimensional mean motions become increasingly prevalent, so that a two-dimensional model (even with variable wavelength) should begin to diverge from experiment.

Thus the high Ra calculations of this study are not expected to be in good quantitative agreement with experiment. However, as can be seen in figure 2 the correlation with experiment is much better than that of the fixed wavelength study, so it is of interest to see how much this correlation could be improved by a more rapid increase of wavelength with Ra. To test the sensitivity of Nu to calculation wavelength, we repeated the $Ra = 6{\cdot}4 \times 10^5$ problem with a mesh of 75×30 cells. The Nu measured in this calculation is shown by the diamond at $Ra = 6{\cdot}4 \times 10^5$. Relative to the difference between the fixed and variable wavelength calculations, this point represents an 8% increase in Nu for a 25% decrease in wavelength. Thus, the heat flux is not a strong function of wavelength for wavelengths near those of figure 1, so that it is not likely that appreciably better correlation could be obtained by a further increase in wavelength.

In figure 2 the calculations that are constrained to be non-turbulent appear to be in better agreement with experiment than the turbulent calculations for $Ra > 2 \times 10^4$. The reason for this is that the neglect of turbulence leads to a

decrease in Nu that counteracts the increased heat flux inherent in the two-dimensional model at large Ra. The convergence to steady state was very slow in these non-turbulent calculations for $Ra > 5 \times 10^4$. In the calculation at $Ra = 1{\cdot}6 \times 10^5$, this slow convergence appeared to be related to the periodic appearance and disappearance of two small counter-rotating eddies associated with the main circulation. A similar development in a non-turbulent calculation at $Ra = 6{\cdot}4 \times 10^5$ resulted in the breakup of the original single circulation into three counter-rotating motions.

4.2. *Turbulence variations with Rayleigh number*

Transition to turbulence occurred for $10^4 < Ra < 2 \times 10^4$ in these calculations. Thus, an initial, low intensity turbulence field decayed away for $Ra < 2 \times 10^4$, but survived and contributed to an increase in heat flux for $Ra \geqslant 2 \times 10^4$. The same transition was observed in the fixed and variable wavelength calculations.

In comparing this transition Rayleigh number with that observed experimentally in air, it is important to distinguish between the 'time-dependent' motions that can be resolved in these two-dimensional calculations and those that cannot. As discussed in § 2.2, it is not possible to resolve such three-dimensional motions as the migration, changes in shape and sinuous oscillations of the rolls. This would require a three-dimensional solution. The onset of turbulence in this numerical study does not, therefore, correspond to the first experimental evidence of unsteady motion. Instead, it should correspond to the first experimental occurrence of local fluctuations, not directly related to the large roll motions. The first local, uncorrelated motions reported by Willis & Deardorff (1970) are 'short length, isolated sharp-crested waves' that maintain their identity for only a short period of time, and are observed for $Ra > \sim 1{\cdot}2 \times 10^4$. These authors report that turbulence is well established in air at $Ra = 3 \times 10^4$. Thus, to the extent that these calculations can resolve time-dependent motions, the onset of turbulence is in good agreement with experiment.

Figure 3 shows the variation of kinetic energy with Ra. The two solid lines in figure 3(a) show the turbulence energy and the total kinetic energy of the flow summed over the calculation region, while the hollow circles indicate the kinetic energy measured in calculations that were constrained to be non-turbulent. The dashed line gives the kinetic energy obtained from a half power law fit to the vertically averaged velocity magnitudes of Malkus (1954) and Deardorff & Willis (1967), presented by the latter authors. For comparison, the averaged experimental measurements have been weighted by the number of calculation cells appropriate for that Ra (see figure 1). As expected, the two-dimensional calculations are more energetic than the real three-dimensional flows, and this discrepancy increases with Ra.

Several discontinuities are apparent in the turbulence energy plot of figure 3(a). Corresponding breaks are also evident in figure 3(b), which compares the maximum value of the three normal components of the Reynolds stress. These discontinuities, which occur at approximately $Ra = 5 \times 10^4$, 2×10^5 and 5×10^5, are related to changes in slope of the heat flux curve to be discussed below. They

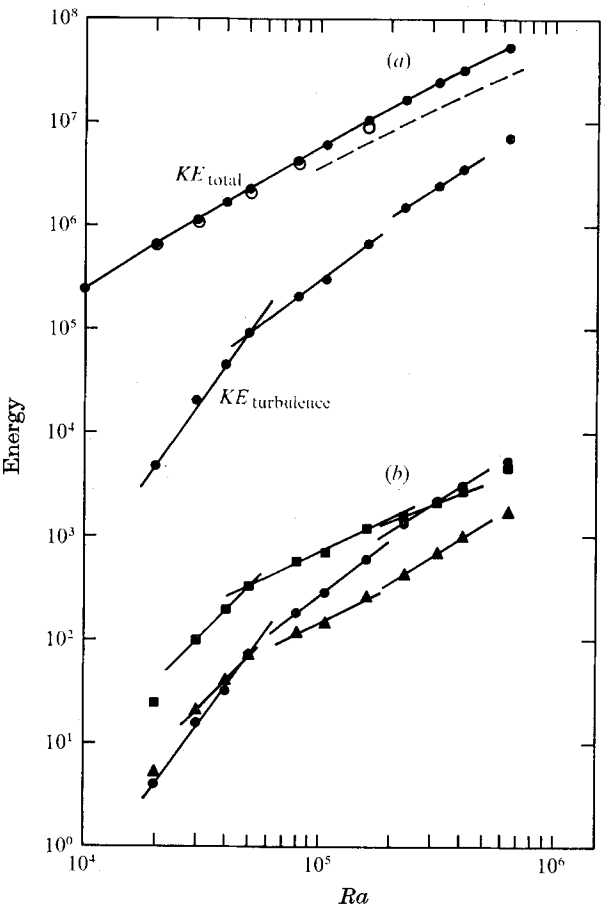

FIGURE 3. (*a*) Variation with Ra of the turbulence energy and the total kinetic energy with (—●—) and without (○) turbulence. ------, fit to experimental data of Malkus, Deardorff and Willis. (*b*) Variation with Ra of the maximum value of the normal components of the Reynolds stress: ●, R_{11}; ▲, R_{22}; ■, R_{33}. The straight lines through the turbulence data show discontinuities at approximately $Ra = 5 \times 10^4$, 2×10^5 and 5×10^5.

appear to be associated with the experimental heat flux transitions observed by Malkus (1954), Willis & Deardorff (1967) and Krishnamurti (1970*a*, *b*).

The turbulence energy increases rapidly with Ra, from less than 1 % of the total kinetic energy at $Ra = 2 \times 10^4$ to 13·5 % at $Ra = 6{\cdot}4 \times 10^5$. However, the composition of the energy shifts with increasing Ra, as demonstrated by the increased importance of the 1 component, relative to the 2 and 3 components in figure 3 (*b*). There are two reasons for the increased relative importance of R_{11}.

(i) The tendency for the peak value of R_{11} to occur where the scale s is large, and for the peaks of R_{22} and R_{33} to occur where s is small (i.e. statistically the 1 component of the energy is concentrated in the larger eddies, and the 2 and 3 components in the smaller eddies). For this reason, the transfer of energy from the 3 to the 1 direction, because of the ω term in the pressure–velocity correlation (equation (3)), is large, while the reverse transfer is small.

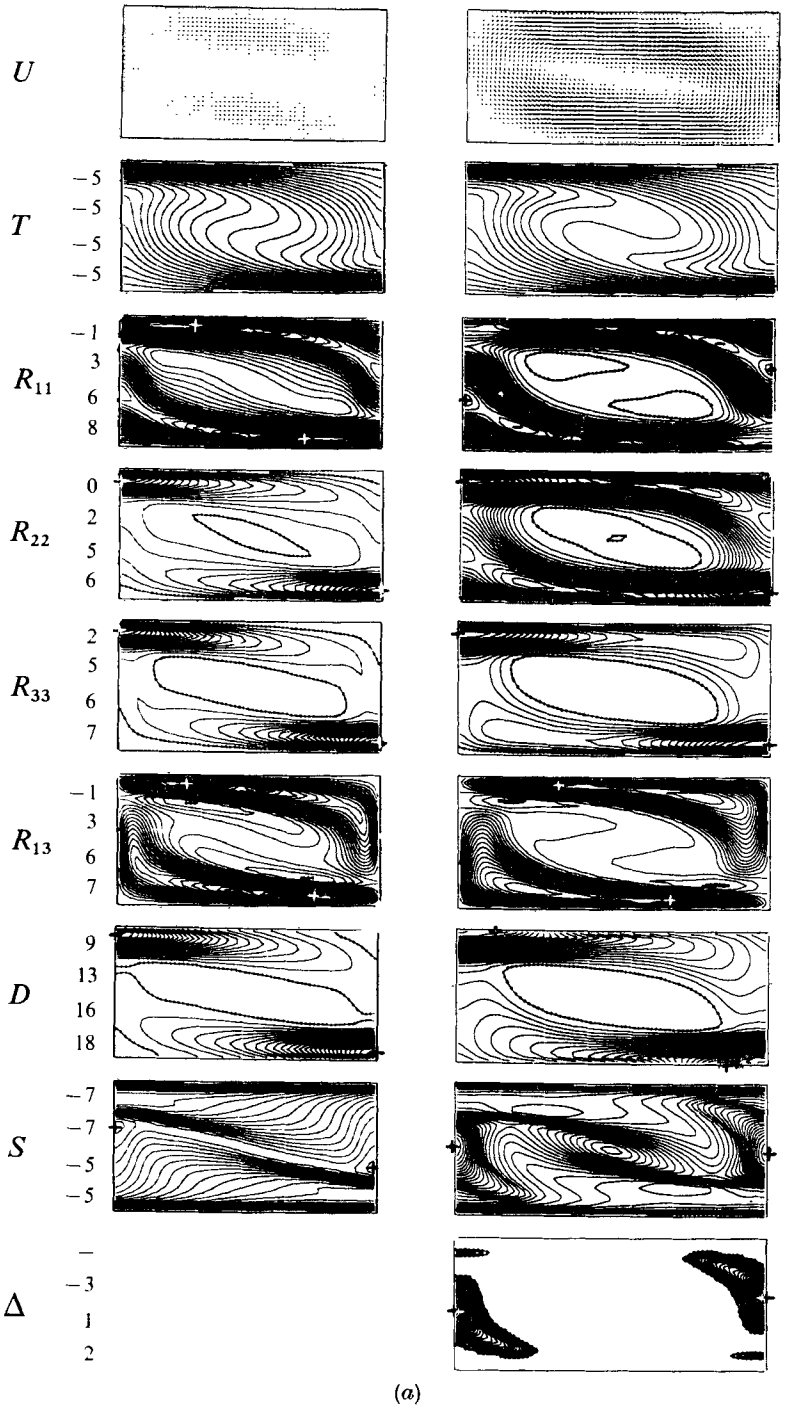

(*a*)

FIGURE 4. For legend see facing page.

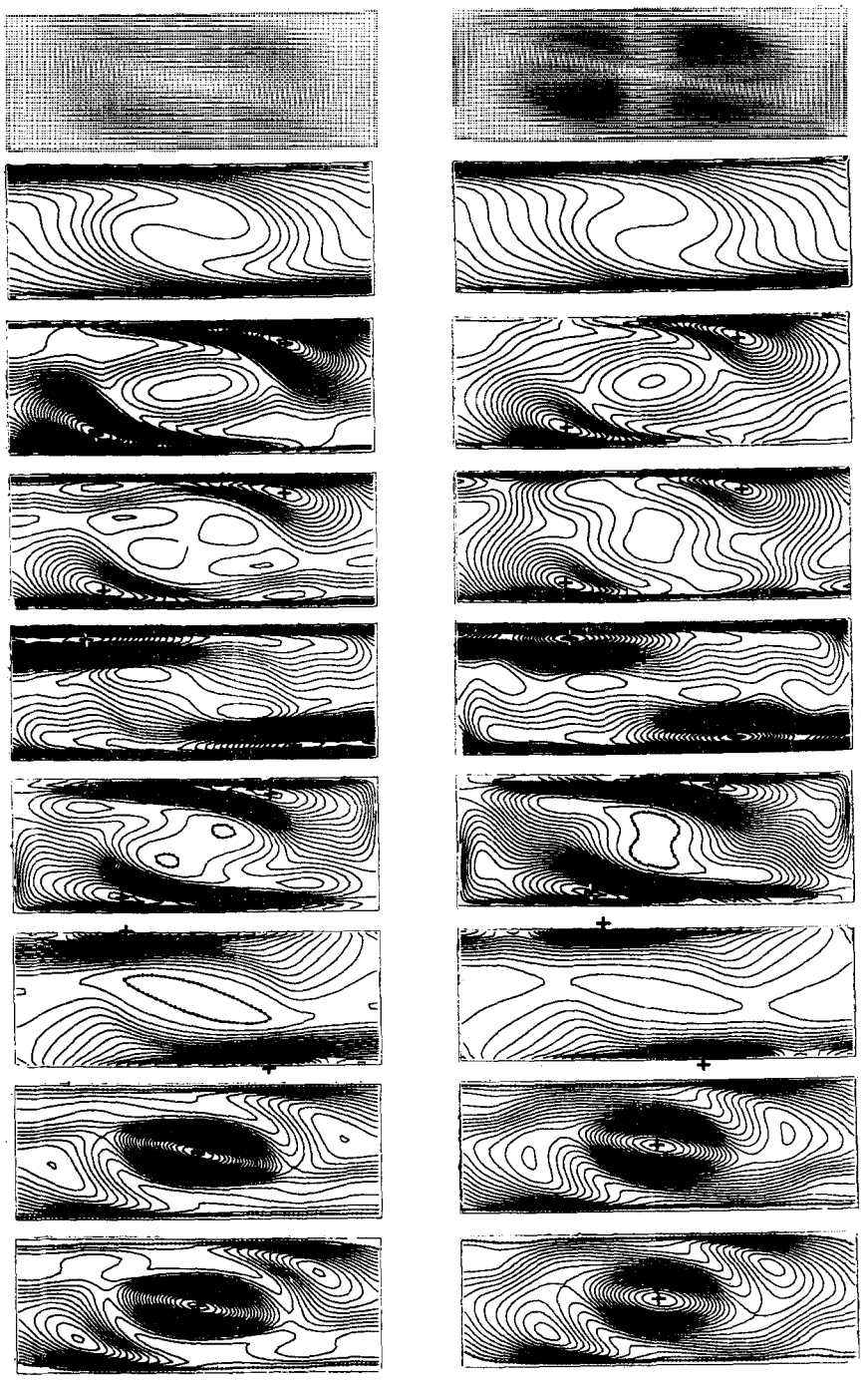

(*b*)

FIGURE 4. Steady-state results at $Ra = 3 \times 10^4$, $1{\cdot}06 \times 10^5$, $3{\cdot}2 \times 10^5$ and $6{\cdot}4 \times 10^5$ (from left to right). The first row of plots show velocity vectors, the remainder are contour plots of temperature T; Reynolds stress components R_{ij}; decay rate D; scale s; and intensity function $\triangle$. The contour intervals are powers of two. The powers are listed at the left in the order in which the plots appear. The + sign indicates a position where the variable assumes its maximum value.

(ii) The increased importance of mean flow shear, relative to buoyancy, as a driving force in high intensity (ξ large) turbulence.

These and other effects of changes in Ra are examined in figure 4. This figure shows the details of the calculated mean flow and turbulence field at steady state for $Ra = 3 \times 10^4$, $1{\cdot}06 \times 10^5$, $3{\cdot}2 \times 10^5$ and $6{\cdot}4 \times 10^5$. The first row of plots are velocity vectors, showing the mean flow circulation. These vectors originate at mesh cell centres, so that one can determine their origin by sighting along a horizontal or vertical line of such centres. The magnitude of the flow velocity increases with Ra, while the form of the circulation remains that of a tilted, clockwise rotating roll at all Ra. A shear layer exists along the no-slip horizontal walls, but not along the free-slip vertical walls, which are planes of symmetry.

The remaining plots in figure 4 are contour plots. In these, local maxima are indicated by a + sign and minimum contour lines are marked by asterisks. The contour interval is always a power of two, so that one may easily compare plots. The powers are listed in the first column in the order in which the plots appear. All of the plots in figure 4 were obtained directly from the computer calculation. The only additions are the + symbols.

The temperature T' field associated with the large circulation consists of a plume of warm air rising along the left side of the mesh and the returning cold air on the right side. Where the horizontal plates interrupt these vertical motions, large temperature gradients exist, their magnitudes increasing with Ra. The temperature contours assume a spiral configuration in the strong vorticity region between the plates. There is a tendency for the spiral to become tighter as Ra is increased, but this trend is reversed at large Ra, owing to the diffusive effect of turbulence. Indeed, it appears that the turbulent diffusion of the temperature field provides the mechanism for limiting the wavelength of these circulating flows. This point is discussed in greater detail at the end of §4.2. A vertical profile of horizontally averaged temperature shows a monotonic decrease of average temperature with height in these calculations, in agreement with experimental observations (Deardorff & Willis 1967). In contrast, the profiles obtained from fixed wavelength calculations show a slight temperature inversion near the edge of the boundary layer.

The next three lines in figure 4 show the normal components of R_{ij}. The horizontal component R_{11} receives its energy from shear creation near the horizontal walls, as well as from coupling among the components. This inter-component coupling provides the sole source of energy for R_{22}; therefore its distribution reflects the relative magnitude of R_{11} and R_{33}. Concentrations of R_{33} are found in the upper left and lower right corners of the mesh where temperature and vertical velocity gradients are large, since this component is fed by buoyancy, as well as shear creation.

At low Rayleigh numbers buoyancy effects dominate. This is demonstrated by the large magnitude of R_{33} relative to R_{11} and R_{22} (notice the contour intervals at $Ra = 3 \times 10^4$ in figure 4), and by the fact that peak values of the latter quantities occur near the R_{33} peak as a result of the transfer of energy from that component. At higher Ra, shear creation becomes a much more important source of turbulence, eventually exceeding the contribution from buoyancy. For

$Ra > 3 \times 10^4$, this is demonstrated by the increased magnitude of R_{11} relative to R_{33} (see also figure 3 (*b*)), the occurrence of the peak R_{11} at a point downstream (as a result of convection) of the region of large horizontal shear, and by the increased similarity of R_{22} to R_{11}.

The character of the turbulence changes sharply when the flow enters the high intensity regime ($\xi > 5$). A consideration of the parameter values, (9) and (10), together with (1) and (2), shows that the rate of decay of D relative to that of R_{ij} is such as to produce a discontinuous decrease in $D/q = \Delta/s^2$ at $\xi = 5$, neglecting all other contributions. This change in value of Δ/s^2 has important consequences for many of the terms of (1)–(6). It produces more diffusion of the turbulence quantities and the temperature, less decay and intercomponent coupling, and less creation of D through shear effects (especially since $g(\xi)$ also decreases at $\xi = 5$). On the other hand, D creation through buoyancy is enhanced as a result of the increase in $f(\xi)$ at $\xi = 5$. Since any change in D, the turbulence energy decay rate, produces an opposite change in R_{ij}, the net effect of this shift from low to high intensity turbulence is to emphasize the importance of shear relative to buoyancy in the creation of R_{ij} and to reduce the decay of R_{ij} relative to its creation.

The effect of these changes is evident in figure 4, where the occurrence of high intensity turbulence is indicated by the $\Delta(\xi)$ plots. These plots show that the turbulence development in this buoyancy-driven flow evolves through three stages of intensity, the transitions of which seem to be associated with observed heat flux transitions (§ 4.4). These stages are: (i) a low intensity regime, such as the flow at $Ra = 3 \times 10^4$, where $\Delta = 5$ everywhere; (ii) a regime where the turbulence is of high intensity only where peak values of the turbulence energy are attained, such as for $Ra = 1{\cdot}06 \times 10^5$; (iii) a high intensity regime throughout, as occurs at $Ra = 3{\cdot}2 \times 10^5$ and $Ra = 6{\cdot}4 \times 10^5$. The transition from regime (i) to regime (ii) occurs when the temperature gradients near the walls are sufficiently great to produce a very localized region of high intensity R_{33} creation. The transition from regime (ii) to regime (iii) occurs when the strength of the shear layer near the walls is sufficiently great to produce high intensity R_{11} and R_{13} creation. Because of the increased relative importance of shear creation at high intensity, the turbulence energy increases very rapidly after this transition, and the entire flow field becomes of high intensity.

The creation terms in the D equation closely resemble those of the R_{33} equation, so there is a strong correlation between these two fields. However, D is strongly influenced by the boundary condition (8), so that it is more closely confined to the rigid plates. This is particularly true for high intensity turbulence, where the D field is dominated by a balance between a greatly increased decay term (discussed above) and the diffusion of D through the rigid wall. The change in the distribution of D with Ra leads to a corresponding change in the scale s. The scale tends to be large where D is small and q is large. This corresponds to the mid-channel region and especially those parts of the mid-channel region where R_{11} is large. This accounts for the strong correlation in figure 4 between large values of s and large values of R_{11} for $Ra \geqslant 3{\cdot}2 \times 10^5$. Thus, the large turbulent eddies have a strong x component of momentum, while the smaller eddies are

confined closer to the wall and have a large z component of momentum. There is also a strong correlation between regions of strong turbulent shear stress R_{13} and large values of s, indicating that the large eddies are non-isotropic. The turbulent shear stress also receives a contribution from a buoyancy term proportional to $\partial T/\partial x$. This accounts for the extension of the R_{13} maxima along the sides of the mesh.

The transition from the flow at $Ra = 3{\cdot}2 \times 10^5$ to that at $Ra = 6{\cdot}4 \times 10^5$ is characterized by enhanced shear creation and a more complete confinement of the strong D field to the near vicinity of the rigid walls. This results in a sharp increase in the turbulence energy, shear stress and scale, which effects, in turn, produce a greatly enhanced diffusion of the turbulence fields and the temperature. In particular, the scale is much increased in those regions near the wall where R_{33} attains its peak value. This leads to considerable broadening of the R_{33} peak and increased transfer of heat through turbulence from the near wall region to the mid-channel region.

The greatly increased turbulent diffusion that is apparent at $Ra = 6{\cdot}4 \times 10^5$ has a limiting effect on the wavelength of the circulation. Thus, in figure 4, the velocity vector plot at this Ra indicates a preferred circulation wavelength that is *less* than the wavelength permitted by the width of the computation mesh. This appears to be a consequence of the turbulent smoothing of the temperature field in the mid-channel region, particularly in the relatively uniform temperature, central core region. This has the unusual (for a diffusion process) effect of *increasing* the temperature gradient, and thereby the buoyancy force, at the centre of the circulation. This adds a vertical acceleration to the velocity field at a point closer to the centre of the circulation than would otherwise occur, and results in a shorter circulation wavelength.

As a result of the shortened wavelength of the large-scale motions, the region of maximum shear creation of R_{ij} occurs closer to the horizontal centre of the mesh. Thus the peak values of all components of R_{ij} (particularly R_{33}) are more centrally located at $Ra = 6{\cdot}4 \times 10^5$ than at lower Ra in figure 4.

4.3. *Heat flux transitions: comparison with experiment*

Experimentalists (Malkus 1954; Willis & Deardorff 1967; Krishnamurti 1970*a*, *b*) observe six distinct flow transitions in convective flow between rigid horizontal plates in the Rayleigh number range $1{\cdot}7 \times 10^3$–$1{\cdot}0 \times 10^6$. These transitions appear as discontinuities in otherwise linear segments of plots of $Nu \times Ra$ against Ra. While there is considerable discrepancy among experimenters (and even between different experiments in the same study) regarding the details of these slope discontinuities, there is little doubt that they exist and exhibit a certain basic consistency for a wide variety of fluids. However, the physical processes that produce these transitions are not well understood, especially in the turbulent regime. The transition Rayleigh numbers measured by these investigators are listed in table 1, with the fluid Prandtl number indicated in parentheses.

The first transition in table 1 corresponds to the onset of convective flow, and appears to be independent of Pr. There is an uncertainty in both the Rayleigh number and the interpretation of the second transition. Malkus reported that

Transition	Malkus	Willis & Deardorff	Krishnamurti
1	1 700 (6·7)	1 750 (0·71)	—
2	—	8 200 and 24 000 (0·71)	4 000 (0·71)
	11 000–26 000 (6·7)	11 000–26 000 (6·7)	17 000 (6·7)
	—	21 000 (450)	17 000–22 000 (57–8 500)
3	—	56 000 (0·71)	—
	55 000 (6·7)	—	36 000 (6·7)
	—	54 000 (57)	51 000 (57)
	—	—	56 000 ($\geqslant$ 100)
4	170 000 (6·7)	180 000 (0·71)	180 000 (100)
5	425 000 (6·7)	410 000 (0·71)	—
6	860 000 (6·7)	830 000 (0·71)	—

TABLE 1. Rayleigh number of experimental flow transitions

the transition Ra varied in successive experimental runs, but that visual observations established that the flow became turbulent within the indicated range of Ra. Krishnamurti showed that the lack of reproducibility is related to the history of the flow: transition occurs at a higher Ra if measurements are taken while increasing rather than decreasing Ra. However, she correlated this transition with the appearance of laminar, three-dimensional convection. In this she is supported by the findings of Willis *et al.* (1971), who related this transition to changes in the rate of growth of circulation wavelength with Ra, which they claimed also coincides with the appearance of laminar bimodal convection. These are the transitions at Prandtl numbers of 6·7 and 450 in table 1. In the case of air, there is an additional correlation between a change in the rate of growth of the circulation wavelength at $Ra = 8200$ and Willis & Deardorff's (1967) heat flux transition at the same Ra. These authors do not correlate the transition in air at $Ra = 24\,000$ with any visual observations; but in Willis & Deardorff (1970) it is indicated that turbulence is well established in air at $Ra = 30\,000$.

There is better agreement among the investigators regarding the higher Rayleigh number transitions, although Krishnamurti observed a greater variation with Pr at the third transition. She correlated this transition with the appearance of a laminar time dependence characterized by a slow tilting of the rolls and the circulation of high-shear regions about the rolls. Malkus, on the other hand, identified transitions 3–6 as shifts from one mode of turbulence to another.

In this numerical study we have observed transitions in heat flux that can be correlated with the experimental transitions 2–5 (transition 1 is at a Ra smaller than those considered here) of table 1. These are shown in the plots of $Nu \times Ra$ against Ra of figures 5–7. As in the experimental studies, the data points have been fitted by a series of straight line segments, the intersections of which mark the transition points. These transition points are in good correlation with the changes in slope of the turbulent data shown in figure 2. In addition to the results obtained in the turbulent calculations, figures 5 and 6 also contain $Nu \times Ra$ values measured in the calculations that were constrained to be non-turbulent.

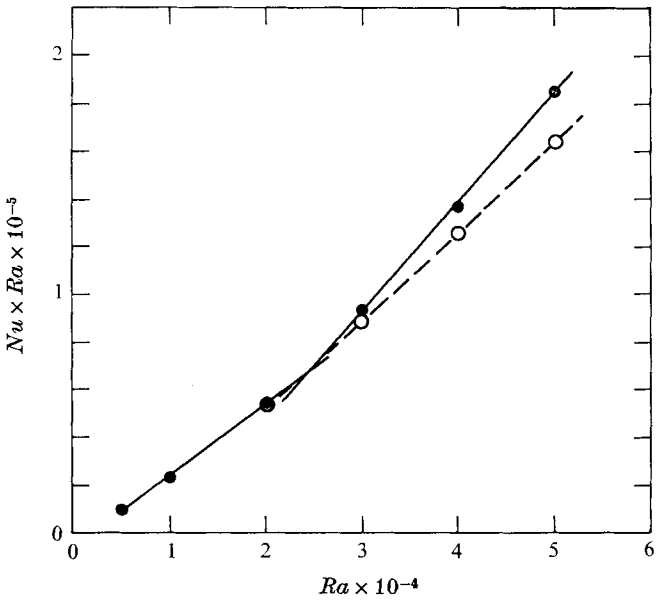

FIGURE 5. Plot of $Nu \times Ra$ against Ra, showing a discontinuity at $Ra = 2{\cdot}5 \times 10^4$; —●—, calculations with turbulence; ---○---, calculations without turbulence.

These non-turbulent data provide a basis for evaluating the role that turbulence plays in the heat flux transitions. They also provide a measure of the curvature that exists in the heat flux plots as a result of the two-dimensional constraint.

The heat flux transition shown in figure 5 at $Ra \approx 2{\cdot}5 \times 10^4$ is probably associated with the onset of turbulence, which occurs at $Ra = 2 \times 10^4$ in these numerical calculations. However, this correlation is somewhat obscured by the fact that there also appears to be a transition in the non-turbulent measurements at this Ra in figure 5. We know of no explanation for this latter transition, and presume that this is not a real change in slope, but simply evidence of the positive curvature that exists in the $Nu \times Ra$ curve, resulting from the two-dimensionality of the calculation. If this is the case, then the uniform departure of the turbulent data points from the non-turbulent ones in figure 5 does mark a true slope transition at $Ra \approx 2{\cdot}5 \times 10^4$. This point is in good agreement with Willis & Deardorff's transition measured in air at $Ra = 2{\cdot}4 \times 10^5$, and with the observed Ra for transition 2 (see table 1) measured for other fluids. Willis & Deardorff's transition for air at $Ra = 8200$, and Krishnamurti's at $Ra = 4000$, are apparently related to three-dimensional but non-turbulent phenomena that we cannot duplicate.

Figure 6 shows the second transition observed in this study, occurring in the range $5 \times 10^4 < Ra < 8 \times 10^4$. In this case there can be no confusion regarding the role that turbulence plays in the transition, since the non-turbulent results show no tendency toward a heat flux transition for these Ra. An attempt to determine this transition more precisely by performing a calculation at $Ra = 6{\cdot}5 \times 10^4$ was not successful, because the initial large circulation broke up into three narrow, oppositely rotating circulations at this Ra. This was the only

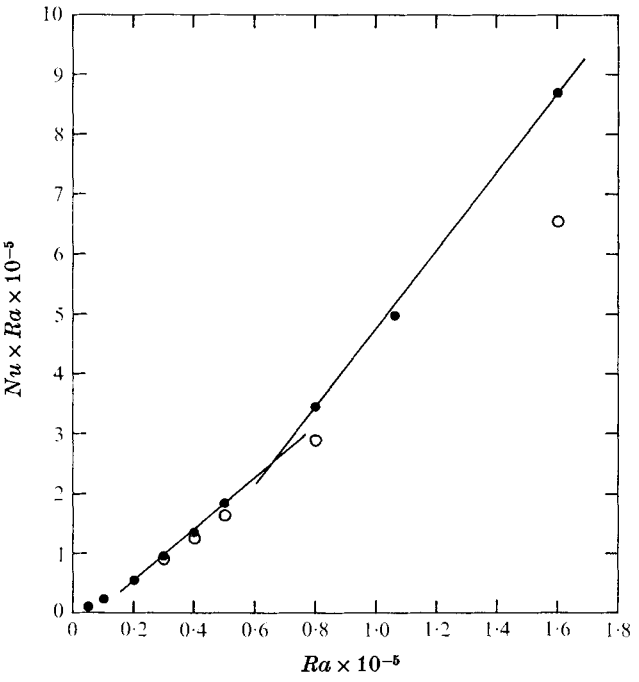

FIGURE 6. Plot of $Nu \times Ra$ against Ra, showing a discontinuity at approximately $Ra = 6 \times 10^4$; —●—, calculations with turbulence; ○, calculations without turbulence.

instance in which this phenomenon was observed in the turbulent calculations (although a similar breakup into three counter-rotating rolls occurred in the non-turbulent calculation at $Ra = 6{\cdot}4 \times 10^5$). The resulting circulation wavelength, $\frac{3}{2}$ the plate separation distance, may correspond to a preferred two-dimensional calculation wavelength. In a study at lower Rayleigh numbers, Lipps & Somerville (1971) report a calculation wavelength less than twice the plate separation when the mesh width was large compared with the wavelength.

The experimental transition number 3 at $Ra = 5{\cdot}6 \times 10^4$, $Pr = 0{\cdot}71$ (table 1) falls within the calculated transition range in figure 6. Similar good agreement is found between experimental transition number 4 and the calculated transition at $1{\cdot}6 \times 10^5 < Ra < 2{\cdot}3 \times 10^5$ in figure 7. There also appears to be a correlation between experimental transition number 5 and a calculated transition between $Ra = 4{\cdot}1 \times 10^5$ and $Ra = 6{\cdot}4 \times 10^5$. There is not sufficient data to determine definitely the $Nu \times Ra$ slope for these values of Ra in figure 7, although an extension of the linear segment fitting the data for $Ra < 4{\cdot}1 \times 10^5$ falls considerably below the $Ra = 6{\cdot}4 \times 10^5$ point. However, more evidence for a turbulence transition in this range of Ra is given by the changes in the details of the flow field, as discussed above in relation to figure 4, as well as changes in the relative contribution of conduction, convection and turbulent diffusion to the heat flux, to be considered below.

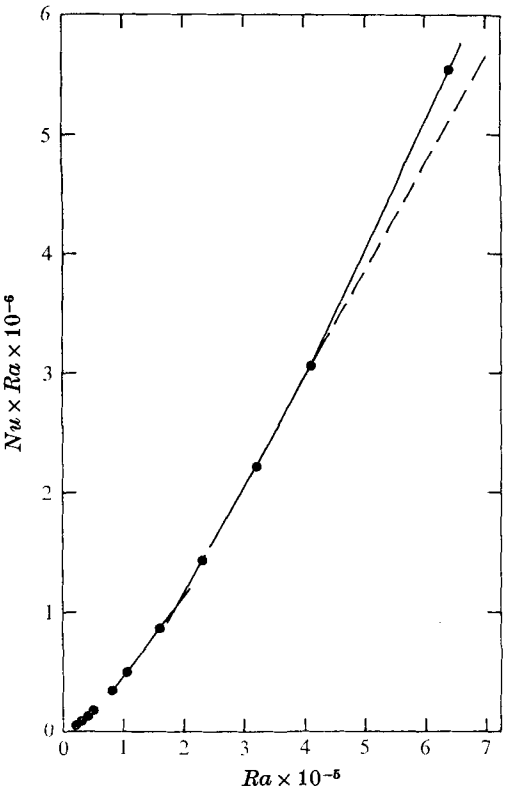

FIGURE 7. Plot of $Nu \times Ra$ against Ra, showing a discontinuity at approximately $Ra = 2 \times 10^5$ and a possible discontinuity between $Ra = 4{\cdot}1 \times 10^5$ and $Ra = 6{\cdot}4 \times 10^5$.

4.4. *Correlation between changes in turbulent structure and heat flux transitions*

To understand the physical processes that give rise to the heat flux transitions seen in figures 5–7, it is useful to examine in greater detail the phenomena that contribute to the heat flux. The Nusselt number at any height z is given by

$$Nu = \frac{1}{L}\int_0^L \Big[\underbrace{u_z T}_{\text{convection}} \quad \underbrace{-\frac{\partial T}{\partial z}}_{\text{conduction}} \quad \underbrace{-\frac{\tau s^2}{\Delta}\left(R_{33}\frac{\partial T}{\partial z} + R_{13}\frac{\partial T}{\partial x}\right)}_{\text{turbulent diffusion}}\Big]\, dx. \tag{19}$$

Here $L = l/h$ is the dimensionless width of the calculation mesh.

Although Nu is constant in z, the relative importance of the contributors to Nu varies considerably with distance from the plates. In figure 8 we show profiles of the horizontally averaged convection, conduction and turbulent diffusion of heat for each of the Rayleigh numbers considered in figure 4 as well as for $Ra = 10^4$. These values of Ra were chosen to typify each of the regimes of flow that correspond to the linear segments of the heat flux curve in figures 5–7. We shall make use of these profiles, together with the details of the turbulence fields shown in figure 4, to understand the unifying features of each of these flow regimes, and

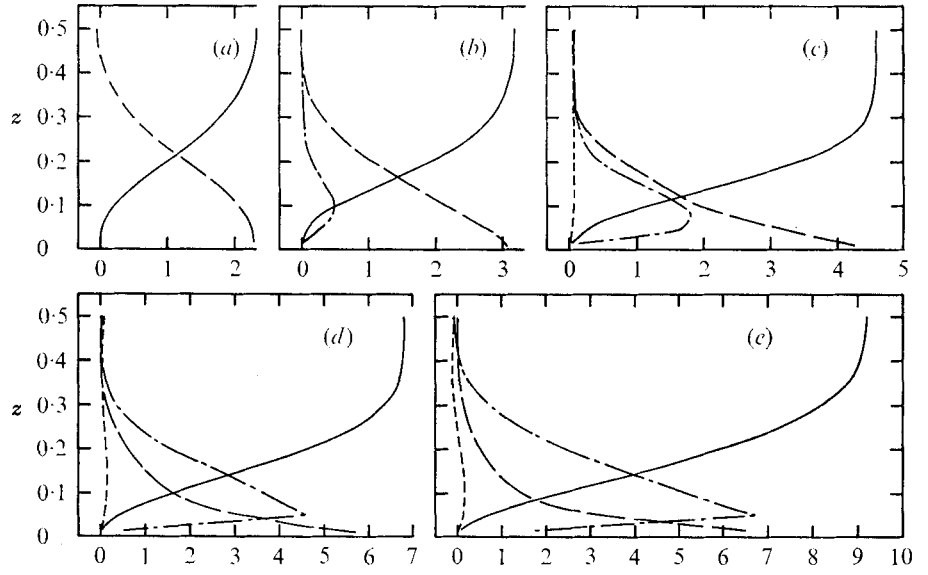

FIGURE 8. Contributions to the heat flux between the plates at various Ra. The curves show profiles of horizontally averaged convection, (——), conduction, (— —), diffusion by turbulent normal stress (— — —), diffusion by turbulent shear stress (— — — —). Ra: (*a*) 10^4; (*b*) 3×10^4; (*c*) $1{\cdot}06\times10^5$; (*d*) $3{\cdot}2\times10^5$; (*e*) $6{\cdot}4\times10^5$.

in this way to explain the changes in flow structure that produce the heat flux transition.

Before considering these transitions in detail, it may be useful to consider the trends indicated in figure 8. The heat flux in the central region between the plates ($z = 0{\cdot}5$) is dominated at all Ra by convection, while conduction is the principal heat transport mechanism near the plates. As Ra increases, the strong convective effect of the large-scale circulation produces greater temperature gradients near the wall, so that the region of important heat conduction is confined more closely to the wall. The heat flux in an ever-expanding region between the plates is dominated by convection and, for sufficiently large Ra, turbulent diffusion. To express this trend in a quantitative way, we show in figure 9 the variation with Ra of the value of z where: (i) the convection profile (figure 8) falls to 98 % of its maximum, (ii) the conduction profile attains 10 % of the value in the calculation cell nearest the wall, and (iii) the R_{33} turbulent diffusion profile reaches 10 % of its maximum on the mid-channel side. Consistent with the phenomenon discussed above, the 10 % maximum conduction curve in figure 9 shows a monotonic decrease in z as Ra increases. The 98 % maximum convection curve displays an initial decrease in z, consistent with the broadening seen in figure 8 between $Ra = 10^4$ and $Ra = 1{\cdot}06\times10^5$, followed by a reversal in trend at $Ra \approx 2\times10^5$ where turbulence begins to exert a much stronger influence on heat flux. The 10 % maximum turbulent diffusion curve is stationary in z for $Ra \lesssim 2\times10^5$, but then increases rapidly as the turbulence enters the high intensity regime.

The heat flux transition that occurs between the flow regimes at $Ra = 10^4$ and $Ra = 3\times10^4$ (figure 8) is easy enough to explain: it corresponds to the onset of

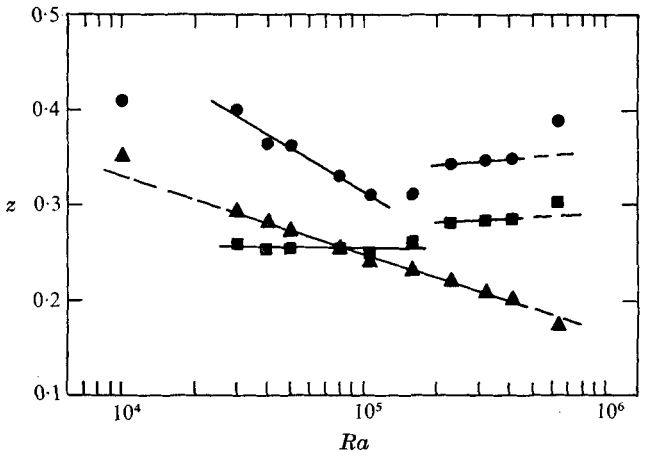

FIGURE 9. A qualitative indication of the variation with Ra of the shape of the profiles of figure 8. The data points mark the value of z where: the convection profile falls to 98 % of its maximum (●), the conduction profile attains 10 % of the value in the calculation cell nearest the wall (i.e. at $z = 0{\cdot}0167$) (▲), the normal stress turbulent diffusion profile reaches 10 % of its maximum (■).

turbulence at $Ra = 2 \times 10^4$. What we should examine in detail, however, is the mechanics by which the details of the turbulence structure influence the change in heat flux at this Ra. We see from (19) that the turbulent flux of temperature is given by $-\tau s^2/\Delta R_{33}\partial T/\partial z$. (The contribution to heat flux by the turbulent shear stress R_{13} is insignificant for $Ra < 1{\cdot}06 \times 10^5$.) At this low intensity turbulent regime $\Delta = 5$ (constant), while τ is always constant, so the heat flux depends on the scale of turbulence (squared), the normal component of the turbulence energy and the normal gradient of the temperature. Thus, from a laboratory standpoint, turbulent heat diffusion corresponds to the convection of temperature from e.g. a warm region to a cool region by a turbulent eddy of size s, moving with velocity $(R_{33})^{\frac{1}{2}}$.

At $Ra = 3 \times 10^4$, R_{33} is concentrated in a narrow region near the rigid plates (figure 4), and the scale of turbulence is small: of the order of the microscale. Therefore, the diffusional power of the turbulence is not large and only a modest transport of heat from the near wall (i.e. outside the laminar sublayer) region to the mid-channel region occurs. The result is a slight increase in heat flux owing to increased temperature gradients in the laminar sublayer, as well as more heat available for convection by the large-scale circulation. Thus, the contribution from heat conduction is increased (figure 8), but confined more closely to the wall (figure 9), while the effect of heat convection occupies a larger part of the mid-channel.

The heat flux transition that occurs between the flow regimes at $Ra = 3 \times 10^4$ and $Ra = 1{\cdot}06 \times 10^5$ has a more subtle explanation than the previous one. The turbulent structure is not much different at the two Rayleigh numbers: R_{33} is still concentrated very close to the plates, and the scale remains small. The primary difference is that the turbulence has entered the high intensity regime in some regions of the flow at $Ra = 1{\cdot}06 \times 10^5$ (notice the $\Delta(\xi)$ plot in figure 4),

and particularly in a small region where the peak value of R_{33} occurs. As discussed in § 4.2, the transition from low to high intensity turbulence results in an increase in turbulent diffusion. The effect of this can be seen in figure 4 as a slight broadening of the R_{33} peak in that region where the turbulence has become of high intensity (see $\Delta(\xi)$ plot). Another effect of the transition to high intensity turbulence has been the more rapid growth of R_{11}, which results in a reduced transfer of energy from R_{33} to R_{11} by inter-component coupling (3). All of these effects combine to increase R_{33}, as well as the diffusion of heat into the region between the plates. Thus a relatively small change in the turbulence structure has produce a noticeable transition in heat flux between the plates.

The change in turbulence structure between $Ra = 1{\cdot}06 \times 10^5$ and $Ra = 3{\cdot}2 \times 10^5$ is major. It results from the development of a mean flow shear layer strong enough to produce high intensity creation of R_{11} and R_{13} (§ 4.2). Because of the increased relative importance of shear creation at high intensity (§ 3.5), the high intensity region spreads very rapidly following this development and soon encompasses the entire flow. This transition produces a sharp increase in turbulent diffusion, the results of which are evident in figure 4 by the widened peaks of all of the R_{ij} components at $Ra = 3{\cdot}2 \times 10^4$ and in figures 8 and 9 by the greatly increased magnitude and extent of the turbulent diffusion of heat. Owing to the increased diffusion of R_{33}, the effect of turbulent heat diffusion is felt closer to the wall, so the region of important heat conduction is quite narrow in figure 8. Likewise, heat is diffused further into the mid-channel region by turbulence, so the strong effect of convection is not felt so close to the walls.

The heat flux transition that appears to occur between $Ra = 4{\cdot}1 \times 10^5$ and $6{\cdot}4 \times 10^5$ (figure 7) can be correlated with an important increase in the shear creation of turbulence at $Ra = 6{\cdot}4 \times 10^5$. As mentioned above, shear creation increases more rapidly with Ra than buoyancy creation in high intensity turbulence, so that by $Ra = 6{\cdot}4 \times 10^5$ the magnitude of R_{11}, which is created through shear, is larger than that of R_{33} and the turbulent shear stress, R_{13}, is sufficiently large to contribute noticeably to the heat flux between the plates. But the more important effect is that the turbulence energy level is increased considerably at $Ra = 6{\cdot}4 \times 10^5$ (figure 3(*a*)), and this produces a larger turbulence intensity. The scale of turbulence in the region of peak R_{33} is now much larger than at $Ra = 3{\cdot}2 \times 10^5$ (figure 4), so that turbulent heat diffusion is greatly enhanced. Although the measurements at $Ra = 6{\cdot}4 \times 10^5$ are probably less accurate than those at smaller Ra (because of residual fluctuations: see appendix A), it is very unlikely that the results mentioned above would be seriously modified by improvements in the accuracy of solution.

The results of § 4.4 are summarized in table 2, which gives the Rayleigh number and explanation of each of the heat flux transitions observed in this study. The transitions are numbered to correspond to the experimental heat flux transitions of table 1.

Transition	Rayleigh number	Explanation
2	1×10^4–2×10^4	Onset of low intensity turbulence
3	5×10^4–8×10^4	Locally high intensity turbulence
4	$1{\cdot}6 \times 10^5$–$2{\cdot}3 \times 10^5$	Uniformly high intensity turbulence
5	$4{\cdot}1 \times 10^5$–$6{\cdot}4 \times 10^5$	Increased intensity, strong shear creation

TABLE 2. Calculated flow transitions

4.5. *Additional comparisons with experiment*

Figures 10 (*a*)–(*c*) show comparisons of vertical profiles of horizontally averaged transverse and vertical components of kinetic energy and mean temperature, respectively, between results of calculations at $Ra = 6{\cdot}4 \times 10^5$ and experimental measurements in air by Deardorff & Willis (1967) at $Ra = 6{\cdot}3 \times 10^5$. The calculated transverse kinetic energy was obtained by averaging the x and y contributions:

$$KE_T = \tfrac{1}{4}(u_1^2 + R_{11} + R_{22}),$$

while

$$KE_V = \tfrac{1}{2}(u_3^2 + R_{33}).$$

Results are shown in figure 10 for calculations that employed a 90×30 cell finite-difference mesh ($\lambda/h = 6$ in figure 1) and a 75×30 cell mesh ($\lambda/h = 5$), to show the sensitivity of these profiles to changes in wavelength.

The experimental transverse kinetic energy in figure 10 (*a*) shows a moderate increase from the mid-plate region toward the wall. The calculated profiles, on the other hand, start from smaller values at mid-channel, but increase much more rapidly toward the plates. This discrepancy is partly real, attributable to neglected three-dimensional effects in the numerical study, and partly related to measuring differences. In the experimental study, the large-scale eddies ($\lambda/h > 5$, according to Deardorff & Willis) have no preferred orientation relative to the horizontally moving sampling probe. Thus, the measured horizontal component of the fluctuating velocity would not in general be the maximum horizontal component, as it is in the two-dimensional numerical calculation. Hence the experimental measurements exhibit a velocity deficiency that, upon squaring, becomes a larger energy discrepancy in figure 10 (*a*).

No such difficulties exist regarding the data of figure 10 (*b*), since the experimental measurements were made in a direction normal to this component. However, there is a different inconsistency in this case. The calculated energy level is less than the experimental value in all but a small region near the wall, which seems inconsistent with the larger calculated heat flux in figure 2. The explanation must be that the two-dimensional large-scale motions, which account for most of the calculated heat flux (figure 8), provide a more efficient heat-transfer mechanism than the real three-dimensional eddies.

The temperature profiles in figure 10 (*c*) show good correlation between calculation and experiment near the wall and mid-channel regions, but the calculations exhibit a rounder shoulder than the experiment. This results from the strong, two-dimensional convection produced in the calculations, which tends to reduce temperature gradients at the edge of the boundary layer.

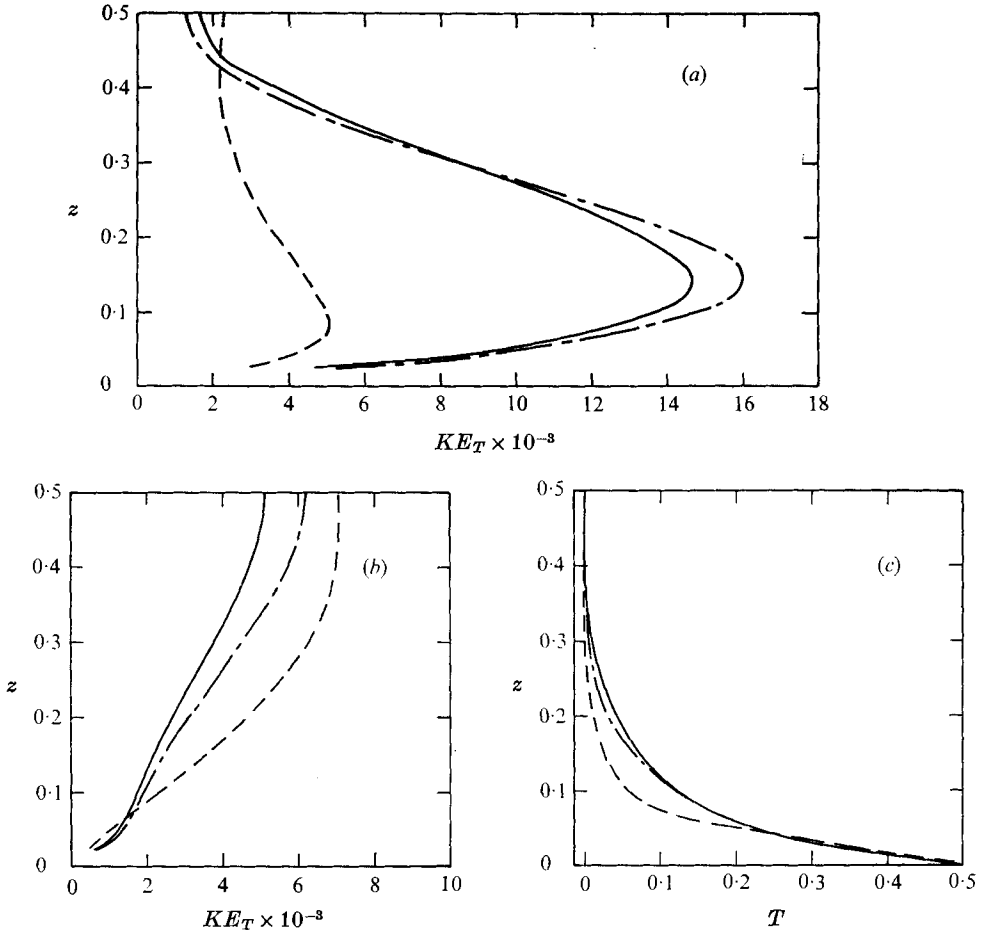

FIGURE 10. (*a*) Comparison of the horizontally averaged transverse component of kinetic energy as measured in numerical calculations at $Ra = 6{\cdot}4 \times 10^5$ and in experiments by Deardorff & Willis (1967) at $Ra = 6{\cdot}3 \times 10^5$. ——, calculation with 90×30 mesh; — — —, calculation with 75×30 mesh; — — —, experiment. (*b*) Vertical component of kinetic energy; otherwise same as (*a*). (*c*) Mean temperature profiles; otherwise same as (*a*).

5. Conclusion

This study is one of a series that have been undertaken for the purpose of developing a universal transport representation of turbulence. The purpose of the present investigation was to examine the validity and applicability of (1) and (2) for calculating the transition from laminar to turbulent flow. A second goal was to examine the flow at higher Rayleigh numbers, to determine if one could observe and explain a series of heat flux transitions that have been detected experimentally.

These calculations are certainly not without their constraints. The most important of these is the inability, owing to computer limitations, to include the effects of three-dimensional variations (the turbulence transport equations do *describe* fully three-dimensional turbulence) in the flow. Computer limitations

also preclude a more detailed spatial resolution of the flow (the sensitivity of results to this parameter is examined in appendix A), as well as a more intensive study of the variation with Rayleigh number. Another inhibiting factor has been the paucity of experimental data that one can use in developing a realistic model of the transition from low to high intensity turbulence. In view of these difficulties, we expect to be able to show only qualitative trends regarding the relationship between heat flux transitions and changes in turbulent structure, although the reasonable agreement with experiment seen in figures 2 and 10 (except for figure 10 (*a*), for which the discrepancy is thought to be understood: see § 4.5) encourages a belief in the validity of these correlations.

The calculations predict a transition to turbulence in the range.

$$10^4 < Ra < 2 \times 10^4,$$

in good correlation with experimental observations (Willis & Deardorff 1970) of the onset of widespread turbulent fluctuations in air. At higher Ra, additional transitions have been observed, and these agree in number and Ra with the heat flux transitions observed experimentally. In the calculations these appear, not only as changes in slope of linear segments of $Ra \times Nu$ plotted against Ra, but also as discontinuities in log–log plots of the variation with Ra of the total turbulence energy and the maximum of each component of the turbulence energy.

Four turbulence transitions have been detected in the calculations (table 2), and each of these has been found to correspond to a change in the calculated turbulent structure. These four structural classes can be described as: (i) an initial, low intensity turbulence; (ii) a low intensity turbulent field with local regions of high intensity; (iii) uniformly high intensity turbulence; (iv) increased intensity through strong shear creation. The transfer from one structural class to another is shown to be accompanied by changes in the relative contribution of conduction, convection and turbulent diffusion to the heat transfer between the plates. Thus we can correlate changes in the turbulent flow structure with changes in the heat flux mechanism, and these in turn can be related to the observed heat flux transitions. The good correlation between calculated and experimental heat flux transitions encourages one to believe that the calculational limitations mentioned above do not preclude a similar explanation for the heat flux transitions that are observed in the laboratory.

This work was performed under the auspices of the United States Atomic Energy Commission, and was partly supported by the Office of Naval Research, Government Order NAonr-2-73. The author would like to thank Dr F. H. Harlow for his continuing interest in this study and many helpful discussions.

Appendix A. Details of the numerical calculations

Despite the title of this appendix we do not present here detailed finite-difference formulae or solution algorithms for (1)–(6), since the numerical methods employed in this study are straightforward extensions of previously documented procedures. For additional information on these points, the reader is referred to

Daly & Harlow (1970) and Amsden & Harlow (1970*a*, *b*). In this section we consider the form of the initial conditions for the calculations, the test for convergence to steady state, the stability and accuracy of the solution technique and the time scale of the calculations. All are important questions that bear on the practicality and the scope of the study.

The starting conditions were chosen in such a way as to hasten convergence to steady state and to avoid initial, large oscillations of the turbulence quantities. The initial velocity field was patterned after Chandrasekhar's (1961, p. 44) result for infinitely long rolls, while the temperature varied linearly in the region between the plates. The turbulence quantities were chosen to be symmetric about the mid-line $z = 0{\cdot}5$ and constant in x, such that

$$R_{33}(z) = 4\,Ra\,(|z-z_w|)^{\frac{4}{3}} \times 10^{-5},$$
$$R_{11}(z) = R_{22}(z) = 0{\cdot}25 R_{33}(z),$$
$$R_{13} = 0{\cdot}0,$$
$$s(z) = \begin{cases} 0{\cdot}8\,|z-z_w| & \text{for} \quad |z-z_w| \leqslant 0{\cdot}25, \\ 0{\cdot}2 & \text{for} \quad |z-z_w| > 0{\cdot}25, \end{cases}$$

where z_w is the value of z at a wall. The initial D is calculated from $D = \Delta q/s^2$. These starting conditions were found to produce a smooth development of the turbulence fields.

Not all of the problems were initiated in this way. In some fixed wavelength calculations a purely laminar flow problem was calculated first, then a turbulence field like the above was introduced and the problem was allowed to evolve to a new steady state. Also, steady-state turbulent solutions at other Rayleigh numbers were sometimes used as starting conditions to hasten convergence. In several cases, problems were initiated in more than one way to test the sensitivity of results to initial conditions. It was found that, to within the convergence criterion, the steady-state results were independent of starting conditions.

The convergence criterion for both laminar and turbulent flow calculations is based on the constancy of the Nusselt number

$$Nu = u_3 T - \left(1 + \frac{\tau s^2 R_{33}}{\Delta}\right)\frac{\partial T}{\partial z} - \frac{\tau s^2 R_{13}}{\Delta}\frac{\partial T}{\partial x}.$$

The average value of this number over a row of calculation cells was computed each time cycle for a row near the wall and another at mid-channel. These Nusselt numbers oscillated with a rather uniform frequency and an amplitude that was damped with time. The calculation was said to have reached a steady state when

$$\max\left[\frac{\langle Nu\rangle^{n+1} - \langle Nu\rangle^n}{\frac{1}{2}(\langle Nu\rangle^{n+1} + \langle Nu\rangle^n)}\right] < 0{\cdot}01\,\delta t, \tag{20}$$

where δt is the time increment and $\langle Nu\rangle^n$ is an average Nu at time cycle n. This criterion was satisfied for all square mesh turbulent flow calculations, but some long-wavelength problems were terminated early, to save computer time.

Statistics for the variable field length calculations are presented in table 3.

Ra	Cells	δt	Time of calculation (min)	Cycles of calculation	$\left(\frac{\delta Nu}{\delta t}\right)_{\min}$	Time/ cell/ cycle (μs)
		Non-turbulent calculations				
5×10^3	1 320	$2{\cdot}5 \times 10^{-4}$	5·4	3 182	0·01	77
1×10^4	1 620	$2{\cdot}5 \times 10^{-4}$	6·7	3 254	0·01	76
2×10^4	1 740	$2{\cdot}5 \times 10^{-4}$	8·0	3 542	0·01	78
3×10^4	1 800	$2{\cdot}5 \times 10^{-4}$	10·3	3 928	0·01	87
4×10^4	1 890	$2{\cdot}5 \times 10^{-4}$	12·7	4 162	0·01	97
5×10^4	1 950	$2{\cdot}5 \times 10^{-4}$	15·5	4 390	0·01	109
8×10^4	2 070	$2{\cdot}0 \times 10^{-4}$	59·0	15 596	0·28	110
$1{\cdot}6 \times 10^5$	2 250	$1{\cdot}0 \times 10^{-4}$	59·0	6 189	2·20	254
$6{\cdot}4 \times 10^5$	2 700	$2{\cdot}0 \times 10^{-5}$	39·3	3 010	11·6	290
		Turbulent calculations				
2×10^4	1 740	$2{\cdot}5 \times 10^{-4}$	42·5	2 723	0·01	538
3×10^4	1 800	$2{\cdot}5 \times 10^{-4}$	52·4	2 986	0·01	585
4×10^4	1 890	$2{\cdot}5 \times 10^{-4}$	55·3	2 854	0·01	615
5×10^4	1 950	$2{\cdot}5 \times 10^{-4}$	56·3	2 776	0·01	624
8×10^4	2 070	$2{\cdot}0 \times 10^{-4}$	53·1	2 560	0·01	601
$1{\cdot}06 \times 10^5$	2 130	$1{\cdot}0 \times 10^{-4}$	89·6	4 242	0·14	595
$1{\cdot}6 \times 10^5$	2 250	$\left\{\begin{matrix}1{\cdot}0 \times 10^{-4} \\ 5{\cdot}0 \times 10^{-5}\end{matrix}\right\}$	100·1	4 866	0·01	549
$2{\cdot}3 \times 10^5$	2 340	$5{\cdot}0 \times 10^{-5}$	119·7	5 806	0·02	529
$3{\cdot}2 \times 10^5$	2 430	$3{\cdot}0 \times 10^{-5}$	119·7	5 745	0·04	514
$4{\cdot}1 \times 10^5$	2 520	$3{\cdot}0 \times 10^{-5}$	119·7	5 370	0·07	531
$6{\cdot}4 \times 10^5$	2 700	$1{\cdot}0 \times 10^{-5}$	119·7†	5 290	0·44	503

† Calculation started from a previous solution.

TABLE 3

The first group of problems are non-turbulent calculations; the remainder include turbulence effects. All calculations were started from the initial conditions given above, except for the final one at $Ra = 6{\cdot}4 \times 10^5$, which was started from a solution obtained with different parameter values. The calculations made use of a 30-cell high, but variable width, finite-difference grid (see figure 1), and employed a time increment that was approximately the maximum value consistent with numerical stability. The computation times on the CDC-7600 varied from 5·4 min to 2 h, which was an arbitrary upper limit. Turbulence added measurably to the computation time, as can be seen by comparing the calculation times/cell/time cycle in the final column of the table. However, the total computation time with turbulence is not increased proportionately, since the number of calculation cycles required to satisfy the convergence required (20) is decreased when turbulence is added. Apparently, the diffusional effect of turbulence leads to a more rapid approach to heat flux stabilization.

For problems that reached steady state, the smallest value of the convergence test number $\delta Nu/\delta t$ is 0·01, by (20). A larger value of this term in table 3 indicates residual fluctuations at problem completion time. Consider the turbulent calculations first. Except for the $Ra = 1{\cdot}06 \times 10^5$ problem, which was terminated after

$1\frac{1}{2}$ h rather than the usual 2 h, these residuals show an increase with Ra, indicating a greater time required for convergence as the driving force and the mesh size increase. However, for the calculations at $Ra < 6{\cdot}4 \times 10^5$, it is probable that no noticeable change in measurement would be observed if these calculations had converged. The residual fluctuations in the maxima of the Reynolds stress components are less than 1 % in these problems. The $Ra = 6{\cdot}4 \times 10^5$ calculation, on the other hand, exhibited fluctuations of approximately 10 % at the time it was terminated. Therefore the measurements at this Ra are likely to be less accurate than those at smaller Ra.

The non-turbulent calculations exhibit a much larger variation in the convergence test number than do the turbulent calculations. The convergence criterion is satisfied in all problems for which $Ra \leqslant 5 \times 10^4$, but large errors persist at problem completion time (for which the upper limit is 1 h in the non-turbulent calculations) at larger Ra. At $Ra = 8 \times 10^4$ and $1{\cdot}6 \times 10^5$ these errors are associated with rather uniform amplitude, time-periodic fluctuations in Nu, which may be associated with the tendency to develop secondary, counter-rotating vortices. These secondary vortices are detectable in the calculation at $Ra = 1{\cdot}6 \times 10^5$. In the calculation at $Ra = 6{\cdot}4 \times 10^5$, a similar phenomenon occurred; but in this case the amplitude of the secondary vortices eventually matched that of the primary circulation, so that the initial single roll broke into three counter-rotating circulations.

The computational limitations imposed on this study by stability and accuracy requirements can best be seen by an examination of the truncation errors of (5). Hirt (1968) and Daly & Pracht (1968) have shown that the finite-difference procedure contributes truncation errors of the form

$$-\left(\frac{\delta t}{2}u_1^2+\frac{\delta x^2}{2}\frac{\partial u_1}{\partial x}\right)\frac{\partial^2 u_1}{\partial x^2}-\left(\frac{\delta t}{2}u_3^2+\frac{\delta z^2}{2}\frac{\partial u_3}{\partial x}\right)\frac{\partial^2 u_1}{\partial z^2},$$

to the right-hand side of the x component of this equation. These errors have the form of diffusion terms with coefficients that may be positive or negative, depending upon the size and magnitude of the velocity gradients. However, in these calculations the gradients are sufficiently small that the spatial truncation errors contribute much less than the δt errors.

These δt errors always contribute to the negative diffusion of u_1, and unless δt is chosen sufficiently small that the errors are overshadowed by the true physical diffusion terms

$$\frac{\partial}{\partial x_k}\left(Pr\frac{\partial u_1}{\partial x_k}-R_{1k}\right),$$

an exponentially growing numerical instability will result. This is the condition that forced the reduced time increments in the high Rayleigh number calculations. But while this constraint is sufficient to ensure the stability of the calculations, the truncation errors nevertheless remain large and contribute to a loss of accuracy. This is believed to explain the slow convergence in the high Rayleigh number problems (a particular difficulty in high Ra, laminar flow calculations, where molecular viscosity and heat conduction provide the only physical dif-

fusion). It would be interesting to repeat these calculations, including terms in the mean flow finite-difference equations that would explicitly compensate for the truncation errors, to examine the effect of these inaccuracies on the calculated flow structure and the rate of convergence to steady state.

The stability restriction for the low Rayleigh number calculations is given by

$$\delta t < \frac{\delta x^2 \delta z^2}{2Pr(\delta x^2 + \delta z^2)} = 3.97 \times 10^{-4}$$

for these calculations. Violation of this condition leads to an oscillating, exponentially growing instability (Hirt 1968). Note that the δt limit varies inversely with Pr. Thus calculations with a Pr appropriate to water (6·8), rather than air (0·7), would require an order-of-magnitude increase in computer time. It is for this reason that the present study was confined to a single, low Pr application, even though more extensive experimental data are available for water.

The $Ra = 2{\cdot}3 \times 10^5$ calculation was repeated with a coarser finite-difference mesh, to test the sensitivity of results to spatial resolution. The original mesh of 78×30 cells was reduced by $\frac{1}{3}$ in each direction so that the number of calculation cells was $\frac{4}{9}$ of the number used in the fine-mesh study. Using the same time increment as in the original problem ($\delta t = 5 \times 10^{-5}$), this calculation required 37·4 min and 3997 computation cycles to reach steady state. The computation time/cell/cycle was 540 μs, which is slightly greater than the time required in the fine-mesh problem (table 3). The appearance of the mean flow and turbulence fields is little changed by the change in resolution, but the magnitudes of the turbulence fields shows about a 20 % shift away from shear generated turbulence toward buoyancy generated turbulence in the crude-mesh problem. The total turbulence energy was approximately 30 % lower than the better resolved problem, while the mean flow energy was 3 % higher and the total kinetic energy was essentially unchanged. The Nusselt number was reduced by 4 %. In view of the large change in mesh size, these variations do not indicate a strong sensitivity of results to finite-difference resolution.

Appendix B. Sensitivity of results to variations of parameters

In Harlow & Romero (1969) and Daly & Harlow (1970), the sensitivity of results to variations in many of the parameters of (1)–(3) was examined. Because of the large computation time involved, it is not practical to re-examine all of the effects in the present study, so we limit our attention to the newly introduced parameters, τ, $f(\xi)$ and Ω. The effect of these terms is studied by varying their values from those given in § 3.5 in recalculations of the $Ra = 1{\cdot}6 \times 10^5$ problem. The computations do not reach steady state, but are carried sufficiently far that any residual fluctuations in measured values are likely to be small compared with the variation of the calculated results from the original $Ra = 1{\cdot}6 \times 10^5$ steady state.

At $Ra = 1{\cdot}6 \times 10^5$ the flow is in the intermediate regime between low and high intensity turbulence (see § 4.2). In this regime the turbulence is high intensity only in those parts of the flow where the peak values of the turbulence

Parameter variation	Mean flow energy $\times 10^{-6}$	Turbulent energy $\times 10^{-5}$	Nusselt number	$R_{11,\max}$	$R_{33,\max}$	$D_{\max}$ $\times 10^{-5}$
none	9·83	6·69	5·43	606	1204	4·79
$f(\xi) = 2{\cdot}04,\ \xi \geqslant 5$	10·01	4·21	5·17	444	910	3·56
$g(\xi) = 0{\cdot}96,\ \xi \geqslant 5$	9·90	5·47	5·28	517	1078	4·04
$\tau = 0{\cdot}88$	8·48	19·60	6·56	1156	1789	8·87
$\tau = 0{\cdot}72$	9·63	2·66	4·73	317	842	3·35
$\Omega = 0{\cdot}24$	9·87	6·51	5·42	579	1193	4·72

TABLE 4

energy are attained. Small changes in the turbulence parameters could be expected to convert the flow to either the low or high intensity regime. Therefore, calculations at this Ra provide a severe test of sensitivity to parameter variations.

This was particularly noticeable in the test of $f(\xi)$, the buoyancy creation coefficient in the D equation. In this test, the high intensity value of $f(\xi)$ was increased 20 %, from 1·7 to 2·04, while the low intensity value was unchanged at 1·0. This change resulted in increased creation of D in regions of large temperature gradient. The increased decay level was sufficient to change the flow in those regions from high to low intensity turbulence. High intensity turbulence did persist in some local regions of the mesh where shear creation dominated, but these regions were diminished in size as a result of increased decay. Thus the effect of the 20 % increase in the high intensity value of $f(\xi)$ was to convert a locally high intensity turbulent flow to one that was amost entirely low intensity. Since low intensity turbulence is much less diffusive than high intensity (§ 4.2), the effect of this change was to confine the turbulence more closely to the wall regions and to reduce its contribution to the heat flux.

A quantitative indication of the effect of this change in $f(\xi)$ can be obtained from table 4. The first row in this table gives the values of some measured quantities from steady-state results at $Ra = 1{\cdot}6 \times 10^5$, using the parameter values listed in § 3.5. The second row gives the values obtained when $f(\xi) = 2{\cdot}04$ at high intensity. The principal effect of this change has been to reduce the total turbulence energy as a result of the shift from locally high to almost entirely low intensity turbulence. Roughly the same percentage reduction is seen for the D maximum as for the R_{ij} maxima, despite the fact that the D creation coefficient at high intensity was increased. The reason is that, because of the shift to low intensity, that coefficient has no effect except to preserve low intensity conditions. The Nusselt number has been decreased about 5 % by this change, demonstrating the decreased turbulent diffusion of temperature at low intensity.

For comparison with this test of the buoyancy creation coefficient, we have also calculated a problem in which the high intensity value of the shear creation coefficient in the D equation $g(\xi)$ was increased 20 %. The trend is very similar

to that observed in the $f(\xi)$ test, but the tendency toward low intensity is not as complete in this case. High intensity conditions are maintained in the regions of peak R_{11} and R_{33} creation. The decreased severity of this change, as compared with that of $f(\xi)$, is evidenced by the measured data in the third row of table 4.

The τ term, which we examine next, arises in the flux approximation for velocity–temperature correlations. It appears as a coefficient of the buoyancy creation term in the R_{ij} equation and as a turbulent diffusion coefficient in the temperature equation. Because of this double effect, the results are very sensitive to variations in τ. To examine this sensitivity in some detail, we have performed two calculations, one with τ increased by 10 % and one with τ decreased by 10 %.

When τ is increased by 10 %, from 0·80 to 0·88, there is greatly enhanced buoyancy creation of R_{ij}. This results, not only from the increased buoyancy creation coefficient, but also from the increased temperature diffusion, which permits buoyancy creation far out into the region between the plates. As a result of this change, the flow becomes high intensity throughout the entire region, and this also increases the strength of the turbulent diffusion. The temperature gradients become very uniform in the region between the plates and this produces the reduced circulation wavelength phenomenon observed in the turbulent calculation at $Ra = 6{\cdot}4 \times 10^5$ (see § 4.2). The result is that peak values of R_{ij} occur much closer to the centre of the circulation than in the original calculation at $Ra = 1{\cdot}6 \times 10^5$.

A decrease by 10 % in the value of τ has an effect much like that of increasing $f(\xi)$. The turbulent flow becomes low intensity except in local regions of strong shear creation. The temperature field, largely unaffected by turbulent diffusion, exhibits sharp gradients close to the wall, and a broad uniform value near the centre of circulation. This produces an appreciable decrease in heat flux, as can be seen in table 4. However, the heat flux provides a much less sensitive measurement of the effect of variations in τ on changes in turbulent structure than do some of the other quantities in table 4. The total turbulence energy, for example, shows approximately a factor of 3 variation for a 10 % change (increase or decrease) in τ, indicating the extreme importance of this parameter.

In contrast to this extreme sensitivity of results to variations in τ, the effect of a 20 % increase in the value of Ω is minimal. The effect on the mean flow energy and Nusselt number, as can be seen in table 4, is considerably less than 1 %. Even the turbulence structure is largely uninfluenced by this change, although there is a detectable shift in magnitude from the 1 to the 3 direction. There is also a slight decrease in total turbulence energy. Both of these effects are predictable, since the increase in Ω increases the importance of $\partial u_1/\partial z$ creation of R_{33} and decreases that effect for R_{11} and R_{13}. Since R_{13} appears as a coefficient in the Ω term (3) for R_{11} and R_{33}, the net effect is a decrease in both of these terms.

REFERENCES

AMSDEN, A. A. & HARLOW, F. H. 1970*a* *University of California, Los Alamos Sci. Lab. Rep.* LA-4370.

AMSDEN, A. A. & HARLOW, F. H. 1970*b* *J. Comp. Phys.* **6**, 322.

BATCHELOR, G. K. & TOWNSEND, A. A. 1948 *Proc. Roy. Soc.* A **194**, 527.

CHANDRASEKHAR, S. 1961 *Hydrodynamic and Hydromagnetic Stability.* Oxford University Press.

CHORIN, A. J. 1966 *New York University, A.E.C. Research and Development Rep.* NYO-1480-61.

CHORIN, A. J. 1968 *Math. Comp.* **22**, 745.

CHOU, P. Y. 1945*a* *Quart. Appl. Math.* **3**, 38.

CHOU, P. Y. 1945*b* *Quart. Appl. Math.* **3**, 198.

CROW, S. C. 1968 *J. Fluid Mech.* **33**, 1.

DALY, B. J. & HARLOW, F. H. 1970 *Phys. Fluids*, **13**, 2634.

DALY, B. J. & PRACHT, W. E. 1968 *Phys. Fluids*, **11**, 15.

DEARDORFF, J. W. & WILLIS, G. E. 1965 *J. Fluid Mech.* **23**, 337.

DEARDORFF, J. W. & WILLIS, G. E. 1967 *J. Fluid Mech.* **28**, 675.

HARLOW, F. H. & HIRT, C. W. 1969 *University of California, Los Alamos Sci. Lab. Rep.* LA-4086.

HARLOW, F. H. & ROMERO, N. C. 1969 *University of California, Los Alamos Sci. Lab. Rep.* LA-4247.

HINZE, J. C. 1959 *Turbulence.* McGraw-Hill.

HIRT, C. W. 1968 *J. Comp. Phys.* **2**, 339.

KRISHNAMURTI, R. 1970*a* *J. Fluid Mech.* **42**, 295.

KRISHNAMURTI, R. 1970*b* *J. Fluid Mech.* **42**, 309.

LIPPS, F. B. & SOMERVILLE, R. C. J. 1971 *Phys. Fluids*, **14**, 759.

LUMLEY, J. L. 1970 *J. Fluid Mech.* **41**, 413.

MALKUS, W. V. R. 1954 *Proc. Roy. Soc.* A **225**, 185.

MULL, W. & REIHER, H. 1930 *Beih. Gesundh.-Ingr.* (1), **28**, 1.

NAKAYAMA, P. I. 1972 Ph.D. thesis, Purdue University.

PLOWS, W. H. 1968 *Phys. Fluids*, **11**, 1593.

RODI, W. 1971 *Imperial College (London) Rep.* TM/TN/A/14.

ROSSBY, H. T. 1966 Ph.D. thesis, Massachusetts Institute of Technology.

ROTTA, J. 1951 *Z. Phys.* **129**, 547.

SILVESTON, P. L. 1958 *Forsch. Geb. IngWes.* B **24**, 29, 59.

WILLIS, G. E. & DEARDORFF, J. W. 1967 *Phys. Fluids*, **10**, 1861.

WILLIS, G. E. & DEARDORFF, J. W. 1970 *J. Fluid Mech.* **44**, 661.

WILLIS, G. E., DEARDORFF, J. W. & SOMERVILLE, R. C. J. 1971 *NCAR Manuscript* no. 71–154.